Heterogeneous fracture toughness of aggregate-reinforced materials via efficient mesoscopic modeling

Aram Bahmani[a,†], Farzan Farahmand[b,†], Hadi G. Kouchaki[c,d], Zakiye Nazari[c], Ramin Yousefi Nooraie[e], Mohammad Reza Mohammad Aliha[d,*]

[a] Department of Mechanical Engineering, McGill University, Montreal, Quebec, H3A 0C3, Canada.

[b] Department of Mechanical and Aerospace Engineering, University of Central Florida, Orlando, FL, United States of America.

[c] School of Mechanical Engineering, Iran University of Science and Technology, Narmak 16846-13114, Tehran, Iran.

[d]Welding and Joining Research Center, School of Industrial Engineering, Iran University of Science and Technology, Narmak, 16846-13114, Tehran, Iran.

[e] Department of Mechanical Engineering, Politecnico di Milano, Milano, Italy.

* Corresponding author. Email: mrm_aliha@iust.ac.ir

[†] These authors contributed equally: Aram Bahmani, Farzan Farahmand.

This manuscript has been reviewed and new version is accepted at Cement and Concrete Research.
(doi:https://doi.org/10.1016/j.cemconres.2025.108130)
Please do not cite without checking for the published version.

Abstract

Accurate assessment of fracture toughness in aggregate-reinforced materials, such as concrete, is essential for predicting failure under various loading conditions. Conventional methods rely on homogeneous fracture parameters, overlooking the critical influence of mesostructural heterogeneity. We present a comprehensive framework to quantify heterogeneous fracture toughness by incorporating aggregate-scale features into finite element models. Realistic mesostructures were used to compute geometry factors and *T*-stress variations along the crack front, revealing substantial local variability due to aggregate dispersion and spatial randomness. By integrating these results with previously reported critical fracture loads, we determined lower and upper bounds of heterogeneous fracture toughness. Linear equations were developed to convert conventional homogeneous values into corresponding heterogeneous bounds. These findings underscore the role of mesostructure in defining fracture threshold zones. Our approach provides a generalizable methodology for evaluating fracture behavior in concrete, asphalt, and other aggregate-reinforced composites, with implications for design, performance assessment, and durability.

Keywords: Aggregate-reinforced materials; Mesostructural modeling; Fracture toughness; Geometry factor; *T*-stress

1. Introduction

Aggregate-reinforced construction materials are composite mixtures consisting of non-uniformly dispersed mineral aggregates with irregular shapes and varying sizes, such as gravel, sand, or crushed stone—bonded by cementitious, bituminous, or polymeric matrices [1,2]. Cement and asphalt concretes are among the most widely used examples of these materials. They are constantly exposed to environmental factors, including daily and seasonal thermal fluctuations, freeze-thaw cycles, humidity variations, and water saturation changes. They endure complex mechanical loadings, particularly traffic-induced stresses applied to the concrete overlays and pavements. The presence of air voids, along with various fillers and additives, further influences their mesostructure and mechanical behavior. These combined factors contribute to their susceptibility to deterioration and failure mechanisms. Understanding the fracture mechanics of these materials is therefore crucial for optimizing engineering designs, improving performance, and developing sustainable alternatives tailored to specific applications. Moreover, it plays a key role in accurately determining pavement rehabilitation timing and assessing long-term service life.

The principles of linear elastic fracture mechanics have widely been applied to analyze the failure of these materials, particularly given their brittle behavior in cold and low-temperature conditions, as well as their exposure to demanding environmental and mechanical stresses [6]. Fracture toughness is a key material property that quantifies resistance to crack initiation and propagation. This response is highly sensitive to crack position and loading conditions, which define different fracture modes: Crack opening (Mode I), in-plane shearing or sliding (Mode II), out-of-plane shearing or tearing (Mode III), and intermediate mode mixities [7]. Several test specimens have been developed to characterize these fracture modes for aggregate-based construction materials, including the semi-circular bend [8], Brazilian disc [9], edge-notched disc bend [10], and edge-notched diametrically compressed configurations [11], among others [12-15]. These experimental methods offer valuable insights into material behavior under complex stress states. However, despite being an inherent material property, fracture toughness is

significantly influenced by specimen geometry and loading conditions, quantified by the non-dimensional geometry factors [16,17]. To eliminate these influences, fracture toughness is often determined under conditions where the stress component parallel to the crack faces, known as the first non-singular term in the crack-tip stress field, or *T*-stress, is negligible [18]. This approach is valid for homogeneous materials, where fracture parameters (geometry factor and *T*-stress) depend solely on specimen geometry and loading conditions. However, for heterogeneous materials such as aggregate-reinforced composites, fracture parameters are also affected by the mesostructure [19]. Despite this, nearly all reported fracture toughness values for these materials have been determined using the homogeneous approach, without accounting for mesostructural effects in the calculation of geometry factor and *T*-stress, leading to potentially inaccurate assessments of true fracture toughness.

Several geometry generation and reconstruction techniques have been developed and integrated with mesoscale finite element (FE) modeling to better understand the influence of mesostructural characteristics, such as aggregate dispersion, shape and size variations, volume fractions, interconnections, and air void distribution on the mechanical, thermomechanical, and damage responses of aggregate-reinforced construction materials. Among these techniques, two- and three-dimensional (2D and 3D) digital image processing reconstruction methods, such as X-ray computed tomography, have been widely used to capture mesostructures with high precision [20-24]. Voronoi tessellation-based methods have also been applied in both 2D and 3D [25,26], either independently or in combination with other random aggregate generation algorithms, including the voxel-based method [27], the splining method [28], and the repartitioning-based aggregate generation algorithm [29]. Other random aggregate generation algorithms have been developed to achieve more realistic mesostructures [30-34]. For instance, the convex-concave surface method, combined with the double background grid method for placing processes [35]. Additionally, the 2D convex and concave polygon method [36] and the Monte Carlo material model [37] have also been among other techniques. Beyond 2D approaches, 3D realistic random aggregate generation algorithms [38,39] have been developed to simulate complex mesoscale interactions. The diffuse meshing technique [40] and parametric and morphological characterization

methods [41] have also been integrated with mesoscale FE modeling to improve accuracy in predicting material responses. The 2D aggregate gradation conversion framework, which incorporates a 3D random aggregate method with machine learning models [42], has been introduced to enhance predictive modeling, while a data-mining framework that combines a 3D random aggregate method with FE simulations [43]. Furthermore, a coarse asphalt mastic-based 3D mesostructure model [44] and a polygonal random aggregate generation algorithm [45] have been proposed.

Despite advancements in mesostructural modeling, the influence of mesostructure on the true fracture toughness of aggregate-reinforced materials under different fracture modes remains unexplored. Existing fracture toughness studies predominantly rely on homogeneous material assumptions, overlooking the significant impact of mesostructural heterogeneities on fracture parameters. Furthermore, most mesomechanical models and algorithms are in-house codes that are not commercially available, requiring complex programming and substantial computational resources. Running these models with pre-existing cracked test specimen geometries for fracture parameter calculations using well-established methods, particularly the *J*-integral, is challenging and time-consuming. Therefore, an integrated approach that explicitly incorporates mesostructural effects in fracture toughness measurements is essential for achieving more accurate and reliable assessments of these material systems.

In this study, we developed a comprehensive computational framework to assess the true heterogeneous fracture toughness of multiphase aggregate-matrix concrete by explicitly incorporating mesostructural heterogeneity. Realistic 3D aggregate dispersion mesostructures are generated and voxelated into volumetric meshes, enabling the mapping of distinct material phases within a finite element modeling environment. Custom-developed codes are used to efficiently construct voxel-based heterogeneous models representative of aggregate-reinforced construction materials. The accuracy of these models is verified through detailed spatial statistical analyses and validated via mesomechanical simulations, benchmarked against experimental data from the literature. These mesoscopic models are then used as virtual fracture test specimens, specifically, semi-circular bend (SCB) and edge-notched disc bend (ENDB) geometries, to simulate

crack initiation and calculate key fracture parameters, including geometry factors and *T*-stress, under Modes I, II, and III loading conditions. Using critical fracture loads reported in prior experimental studies, we determine the corresponding heterogeneous fracture toughness values and establish a set of linear transformation relationships to convert conventionally reported homogeneous values into lower and upper bound heterogeneous equivalents. This work underscores the significant influence of mesostructural heterogeneity on fracture thresholds and provides a generalized, transferable methodology for evaluating fracture behavior in concrete and asphalt pavements, as well as other aggregate-reinforced material systems.

2. Mesostructural geometry generation

2.1. Generating aggregates

To generate a realistic multiphase aggregate-matrix concrete mesostructures, we used Rhinoceros 3D and its visual programming language Grasshopper, integrated with Python scripting. The most challenging constituent to model is the non-uniformly dispersed aggregates with irregular shapes, varying sizes, and distinct volume ratios and fractions. We therefore used the Voronoi tessellation technique, a well-established method for generating aggregates [25,27,28]. Either a cubic or cylindrical domain was discretized into tessellated Voronoi cells, each characterized by a maximum length (d_{max}), defined as the greatest distance among its vertices (Figure 1). The cubic domain was used as a representative volume element (RVE) for finite element (FE) mesomechanical modeling, whereas the cylindrical domain was prepared for FE simulations of fracture test specimens, including the semi-circular bend (SCB) and edge-notched disc bend (ENDB) configurations. The aggregates were classified based on sizes commonly reported for typical concrete and asphalt mixtures in the literature [46-48]: Approximately 2.36 mm (size #1), 4.5 mm (size #2), 9 mm (size #3), and 12.5 mm (size #4), with volume ratios of about 28%, 37%, 26%, and 9%, respectively. We selected these four discrete aggregate sizes with minimal size variation to balance geometric realism and computational efficiency. Modeling larger aggregates makes it infeasible to reach higher aggregate volume fractions ($V_f \approx 60\%$), while incorporating smaller aggregates significantly

increases computational cost and complexity, rendering them impractical for finite element mesostructural modeling.

The aggregates with different volume fractions and volume ratios were generated using the PhysX simulation solver within Grasshopper, which required converting the Voronoi-generated aggregates into a mesh format (Figure 1). The aggregates were randomly positioned within the main domain, and a collision process under gravity was simulated, resulting in a realistic non-uniform dispersion. After collision and reaching stable positions under gravitational effects, the final arrangement of the aggregates was exported as standard triangle language (STL) files.

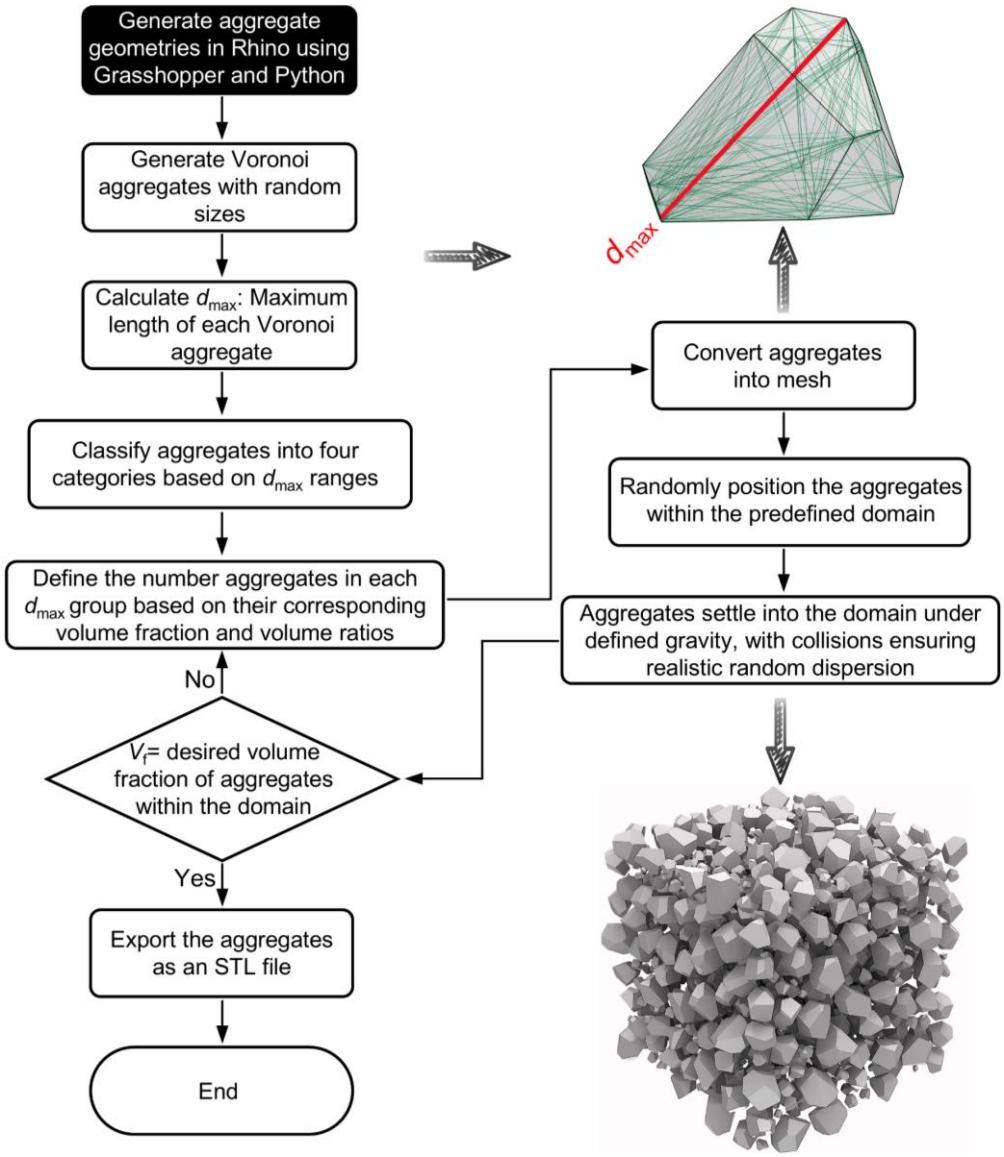

Figure 1: The flowchart of the aggregate generation algorithm integrating Rhinoceros 3D, Grasshopper, and Python scripting.

2.2. Spatial analyses

To quantitatively assess the mesostructural characteristics of the generated aggregates, various statistical functions were applied to evaluate shape irregularity, degree of nonuniformity, and spatial dispersion. For validation and comparison, 3 independent algorithm-generated mesostructural trials and image data from 3 actual asphalt concrete specimens were analyzed (Figure 2a), each with a total aggregate volume fraction of 60%. In the algorithm-generated mesostructures, the volume ratios were chosen to reflect typical gradation used in concrete and asphalt mixtures: 28% for size #1 (2.36 mm), 37% for size #2 (4.5 mm), 26% for size #3 (9 mm), and 9% for size #4 (12.5 mm). The radii and centroid coordinates of the aggregates in both the experimental and simulated specimens were measured using Rhinoceros 3D and Grasshopper software.

2.2.1. Shape irregularity

To characterize the irregularity of aggregate shapes, we defined an isoperimetric shape factor (ISF), a dimensionless index derived from the ratio of a particle's surface area to the surface area of a volume-equivalent sphere. This formulation is based on the concept of *sphericity* originally introduced by Wadell [49], and is expressed as:

$$ISF = \frac{A}{4\pi\left(\frac{3V}{4\pi}\right)^{2/3}} \tag{1}$$

where A is the surface area of the particle, V is volume of the particle, and $(3V/4\pi)^{1/3}$ is the radius of a sphere with the same volume. The denominator $4\pi r^2$ represents the surface area of that ideal sphere. An ISF=1 corresponds to a perfect sphere, while ISF>1 indicates increasing shape irregularity, more surface area than a volume-equivalent sphere. The higher the ISF, the more irregular the aggregate geometry.

Figure 1b presents box-and-whisker plots of the isoperimetric shape factors (ISF) for both algorithm-generated and experimentally measured aggregates. All ISF values exceed 1, indicating that none of the particles are perfect spheres. The algorithm-generated results

exhibit good agreement with the experimental data, capturing the general trend of shape irregularity. However, the experimental aggregates display a broader distribution of ISF values, reflecting a wider range of shape irregularities. This increased variability is attributed to the natural irregularity of real aggregates, whereas the algorithm-generated aggregates were based on four discrete size categories with relatively narrow size variation ranges.

2.2.2. Radial distribution function

The radial distribution function (RDF), g(r) also known as the pair correlation function, offers a long-range spatial analysis of the RVE microstructure. It describes the variation in average aggregate density as function of distance from the centroid of an arbitrary aggregate [50-54]. Specifically, g(r) quantifies how aggregate centers are distributed with respect to one another, relative to a completely random distribution. To compute g(r) the number of aggregates located within a spherical shell of inner radius r and outer radius $r+dr$ is counted, then normalized by the expected number of aggregates in the same shell for a uniform distribution. The mathematical expression is [54]:

$$g(r) = \frac{1}{4\pi r^2 \rho N} \sum_{i=1}^{N} \sum_{j \neq i} \delta(r - r_{ij}) \tag{2}$$

where N is the total number of aggregates, ρ is the average number density of aggregates in the domain, r_{ij} is the center-to-center distance between aggregates i and j, and δ is the Dirac delta function that counts the number of pairs separated by a distance r. Values of g(r)>1 indicate clustering at that distance, g(r)=1 corresponds to a complete spatial randomness (CSR), and g(r)<1 suggests exclusion zones or repulsion.

Figure 2c shows representative radial distribution functions, g(r), for both algorithm-generated and experimental mesostructures as function of the normalized distance r/R_a, where r is the radial distance from the centroid of a reference aggregate and R_a is the aggregate radius. The algorithm-generated results exhibit good agreement with the experimental data, both displaying similarly spaced sharp peaks that reflect consistent spatial ordering of aggregate distributions. These results are further corroborated with

kernel density analysis as function of radial distribution function *g*(r) shown in Figure 2d, where both algorithm-generated and experimental data exhibit similar deviations from the complete spatial randomness (CSR) bound. The complete set of results for all algorithm-generated and experimental trials are presented in Figure S1a-d (Supplementary Material).

2.2.3. Nearest neighbor distance

The nearest neighbor distance (NND) function quantifies the distance between the centroid of each aggregate and that of its closest neighboring aggregate. NND-based functions serve as effective tools for assessing short-range spatial organization and dispersion characteristics within mesostructures [50-54]. To evaluate the degree of spatial non-uniformity, we computed the probability density function (PDF) of the first, second, and third NNDs for all aggregates. In systems with non-uniform dispersion, the first NND PDF typically exhibits a pronounced sharp peak at a value corresponding to the minimum permitted distance between neighboring centroids. The sharpness and intensity of this peak tend to diminish progressively in the second and third NND PDFs, reflecting decreasing local spatial correlations [51]. Furthermore, the range of distances is expected to increase from the first to the second and third nearest neighbor, illustrating the widening spatial separation as the analysis moves beyond immediate neighbors [51]. Figure 2e-g illustrates representative short-range spatial analyses based on the first, second, and third NND for both algorithm-generated and experimental mesostructures. The results indicate a strong correlation between the two, with similar distributions observed across all three NND levels, confirming that the generated mesostructures effectively replicate the local spatial characteristics of actual asphalt concrete. The complete set of NND results for all algorithm-generated and experimental trials are provided in Figure S2a-f (Supplementary Material).

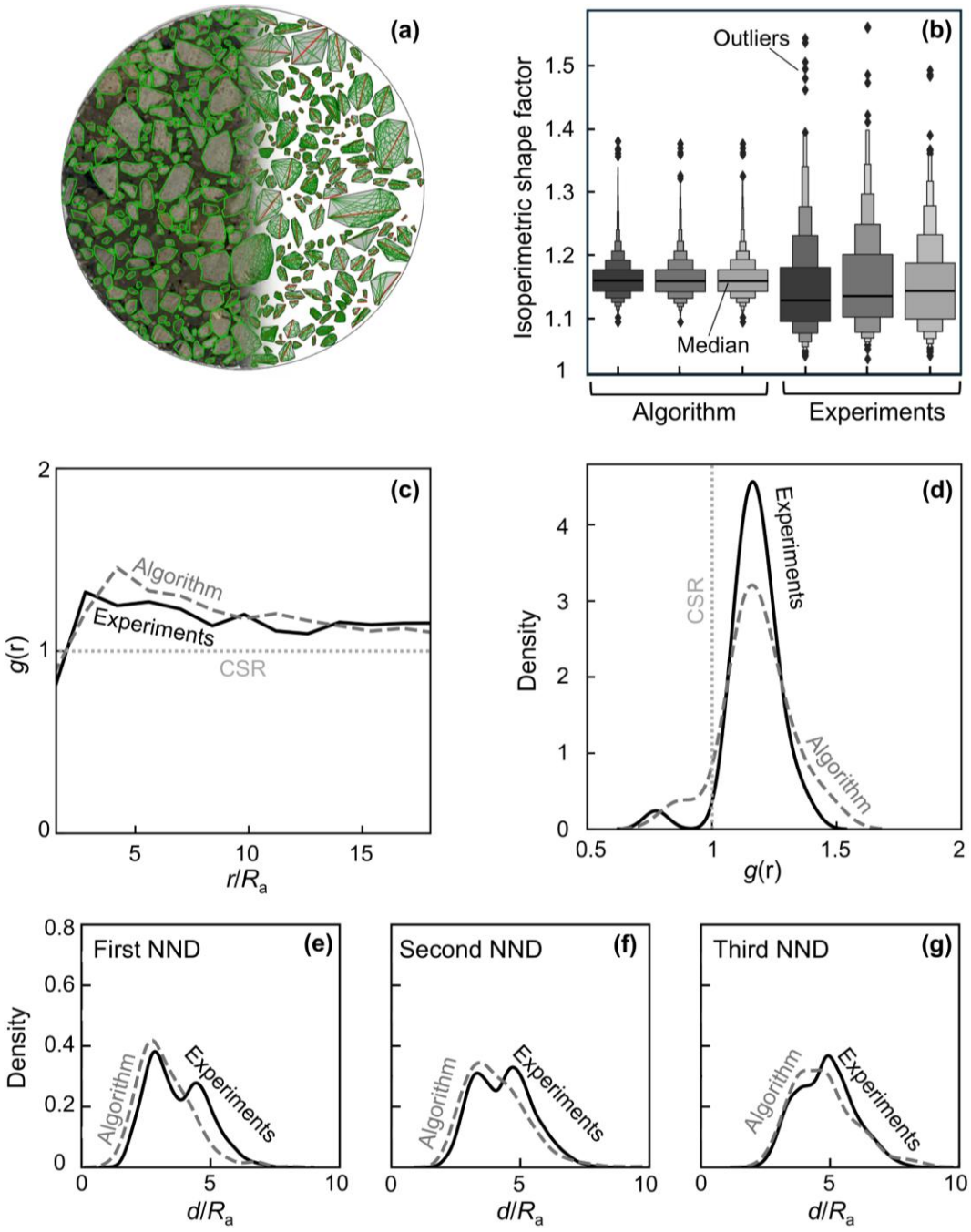

Figure 2: Spatial analysis of experimental and algorithm-generated aggregate distributions, benchmarked against complete spatial randomness (CSR). **(a)** A typical image of experimental and algorithm-generated aggregates; **(b)** box-and-whisker plots of isoperimetric shape factor of experimental and algorithm-generated aggregates; **(c)** radial distribution function g(r) of experimental and algorithm-generated aggregates versus distance normalized by the radius of aggregates (R_a); **(d)** Kernel distribution of the g(r) for experimental and algorithm-generated

aggregates. First **(e)**, second **(f)**, and third **(g)** nearest neighbor distance of experimental and algorithm-generated aggregates.

3. Voxelization and finite element modeling

3.1. Voxelization

Directly using the generated mesostructures with Voronoi aggregates in FE modeling of cracked specimens is computationally intensive, costly, and generally impractical. This is particularly true when computing fracture parameters such as stress intensity factors and *T*-stress, which require specific mesh patterns capable of accurately capturing the singular stress fields near the crack tip. Methods like the *J*-integral are highly sensitive to mesh quality and topology around the crack front, making the use of complex, irregular aggregate geometries nearly infeasible in practice. To overcome this limitation, we developed a hybrid approach that uses the STL-format Voronoi aggregates as templates, which are imported into the commercial FE software ABAQUS and then voxelated through an integrated workflow combining MATLAB programming and custom Python scripts. This process converts each voxel of the Voronoi aggregate into a corresponding volumetric element (Figure 3), enabling efficient and straightforward FE modeling of cracked specimens with multiphase materials or inherent heterogeneity.

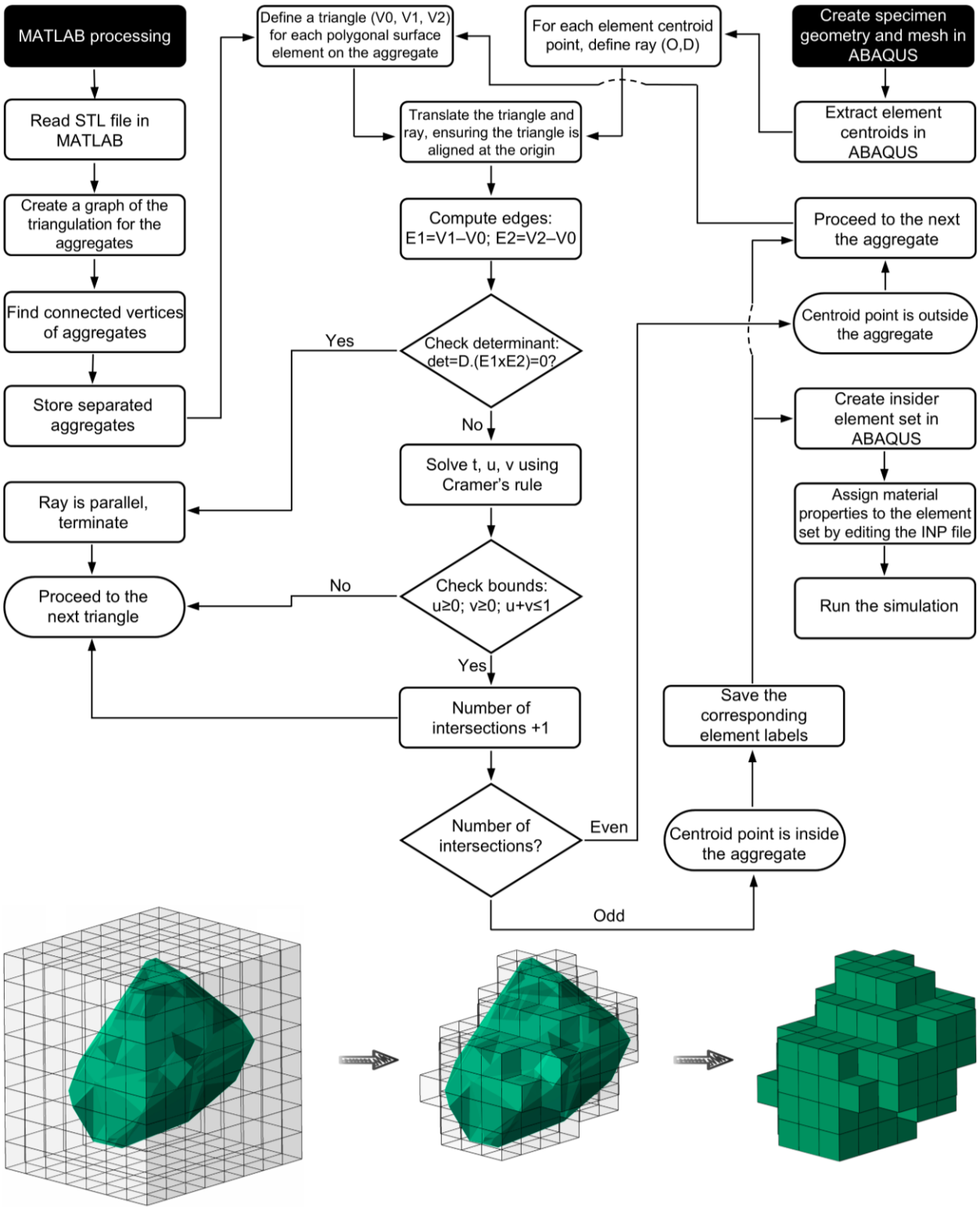

Figure 3: Flowchart illustrating the voxelization process of aggregates and the generation of material-mapped, voxelated aggregate-based finite element models.

The exported STL files from Rhinoceros 3D and Grasshopper contain mesh representations of the aggregates, consisting of node coordinates and associated triangular connectivity data. Each aggregate forms a distinct set of connected nodes. To identify individual aggregates, we parsed the STL file in MATLAB to extract a list of points (vertex coordinates) and their corresponding connectivity information (triangles). Using graph theory analysis, we then identified each aggregate as a connected component within the mesh, allowing each to be treated as an individual triangulation object. To voxelize each aggregate with a finite element mesh, we first duplicated the main domain geometry and meshed it within ABAQUS. A combined Python and MATLAB workflow was then developed to extract the centroid of each finite element and determine which centroids resided within the polygonal surface mesh of any individual aggregate in three-dimensional space. This spatial mapping enabled the assignment of distinct groups of elements as voxelated aggregates based on their geometric inclusion within the corresponding aggregate boundaries (Figure 3). We therefore implemented the fast, minimum-storage ray-triangle intersection algorithm originally introduced by Möller and Trumbore [56] (Figure 3 and 4). This method, widely recognized for its computational efficiency and low memory footprint, was particularly well-suited to our application, which involved extensive point-in-polygon queries across large, mesh-based geometries. A key advantage of this algorithm is that it does not require surface normal vectors, making it robust and independent of the orientation of mesh surface normals. The algorithm operates by casting a ray from each query point in an arbitrary but fixed direction and evaluating its intersections with the target mesh, which is represented as a collection of non-overlapping triangles. Each triangle is defined by three vertices $\mathbf{V}_0$, $\mathbf{V}_1$, $\mathbf{V}_2 \in \mathbb{R}^3$, and the ray is described by an origin (O) and a direction vector (Ψ). The ray is parameterized as (Figure 3 and 4):

$$\mathbf{\Omega}(v) = \mathbf{O} + v\mathbf{\Psi},\ v \geq 0 \tag{2}$$

The core principle of the Möller–Trumbore algorithm is to determine whether and where this ray intersects a triangle surface, without explicitly computing or storing the plane equation of the triangle. This feature makes the method computationally efficient and particularly effective for applications involving large-scale spatial queries. The algorithm

performs a coordinate transformation that repositions the triangle such that one of its vertices is placed at the origin. The remaining vertices then define two edge vectors of the triangle (Figure 3 and 4):

$$\mathbf{K}_1 = \mathbf{V}_1 - \mathbf{V}_0,\ \mathbf{K}_2 = \mathbf{V}_2 - \mathbf{V}_0 \tag{3}$$

The ray's origin is similarly translated:

$$\mathbf{H} = \mathbf{O} - \mathbf{V}_0$$

(4)

The intersection test is reformulated by substituting the ray equation into the barycentric form of the triangle:

$$\mathbf{O} + v\mathbf{\Psi} = (1-u-x)\mathbf{V}_0 + u\mathbf{V}_1 + x\mathbf{V}_2 \tag{5}$$

This leads to a system of linear equations in the scalar parameters v, u, and x, where v is the distance from the ray origin to the intersection point, and u, x are the barycentric coordinates of the intersection point within the triangle. The solution is given by:

$$\begin{bmatrix} v \\ u \\ x \end{bmatrix} = \frac{1}{\det(\mathrm{M})} \begin{bmatrix} \det(\mathbf{H}, \mathbf{K}_1, \mathbf{K}_2) \\ \det(\mathbf{\Psi}, \mathbf{H}, \mathbf{K}_2) \\ \det(\mathbf{\Psi}, \mathbf{K}_1, \mathbf{H}) \end{bmatrix} \tag{6}$$

where M=[$\mathbf{K}_1\mathbf{K}_2$-$\mathbf{\Psi}$] and each determinant represents the scalar triple product of the corresponding vectors. A valid intersection occurs if $u \geq 0$, $x \geq 0$, $u+x \leq 1$and $v \geq 0$. In the context of point-in-polygon testing, an odd number of ray–triangle intersections indicates that the point lies inside a closed surface, while an even number suggests it lies outside. One of the key strengths of this algorithm is its numerical robustness and efficiency in memory usage, as it avoids precomputing triangle normals. This is particularly beneficial for large surface meshes, where memory savings are significant. Furthermore, intermediate computations, such as cross products and dot products are strategically reused, minimizing redundant calculations and further improving performance. To

mitigate issues arising from floating-point precision near triangle planes, we introduced a small epsilon threshold when evaluating the determinant of the system matrix. Rays nearly parallel to a triangle indicated by determinant values close to zero, were discarded early, improving both computational efficiency and numerical stability.

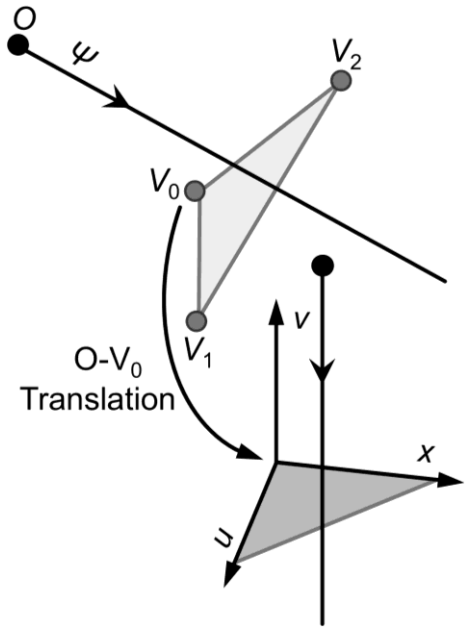

Figure 4: A schematic of Möller and Trumbore fast, minimum storage ray-triangle intersection.

After identifying the finite element centroids residing within the aggregate geometries, a dedicated Python script was developed to read the corresponding element labels and generate an element set in ABAQUS. This element set was then used to assign the aggregate material section by editing the ABAQUS input file accordingly, enabling phase-specific material property definitions within the voxelated domain. A flowchart of the implemented voxelization and FE modeling workflow is presented in Figure 3, while a schematic representation of the Möller–Trumbore ray-triangle intersection algorithm is illustrated in Figure 4.

3.2. Mesomechanical modeling

We assessed the elastic stress states and responses of the generated heterogeneous, aggregate-reinforced mesostructures through mesomechanical finite element modeling.

To evaluate the fidelity of the generated representative mesostructures, we compared the predicted volume-averaged mechanical properties obtained from the FE mesomechanical models with available experimental data for a typical asphalt concrete. This validation was essential for identifying the appropriate stress components to be used in the subsequent calculation fracture parameters, which are critical for accurate fracture toughness measurements. To determine the optimum size of the representative volume elements (RVEs), we generated a series of cubic RVEs with the aggregates volume fraction (V_f) of 60%, edge lengths (L) of 31.25, 62.5, 93.75, and 125 mm, and conducted 3 independent mesostructural trials for each size using our mesostructural geometry generation algorithm (Figure 5a). Each RVE was voxelated using a uniform mesh size of 1.24 mm, resulting in models comprising 15,625, 125,000, 438,976, and 1,030,301 8-node hexahedral (C3D8R) elements, respectively (Figure 5b-c). This range of RVE sizes enabled a systematic investigation of convergence in volume-averaged mechanical properties, thereby ensuring the selection of a statistically representative domain. The elastic properties of the constituent materials were assigned based on reported values [19,48]: the aggregates were modeled with a Young's modulus of E_a=56,800 MPa and a Poisson's ratio of ν_a=0.15, while the matrix was assigned with a Young's modulus of E_m = 13,800 MPa and a Poisson's ratio of ν_m = 0.25. These values are common for cementitious and bituminous based concrete and asphalt mixtures. It was also assumed that the aggregates and matrix were perfectly bonded in the FE models (i.e., coincident nodes were used on the finer-matrix interfaces). Given that this part of study focused on elastic behavior, this assumption was considered appropriate [57-61]. Periodic boundary conditions were applied to the RVEs using node-to-node constraint equations, following detailed techniques described in the literature [57,59]. The implementation of periodic boundary conditions, along with the associated meshing requirements, is further discussed in Ref. [59].

The computed volume-averaged elastic properties of each FE mesomechanical model were obtained through six independent simulations, wherein distinct macroscopic displacements (strains) were applied to the opposing faces of the RVE. In each simulation, a single component of the macroscopic strain tensor was imposed, while ensuring the remaining components were held fixed, allowing for the extraction of

corresponding components of the homogenized stiffness tensor. The relationship between the volume-averaged stress and volume-averaged strain in a heterogeneous material is given by [62]:

$$\bar{\varepsilon}_{ij} = \frac{1}{|\mu|}\int_{\mu_e} \varepsilon_{ij}(x)\, d\mu \tag{7}$$

$$\bar{\sigma}_{ij} = \frac{1}{|\mu|}\int_{\mu_e} \sigma_{ij}(x)\, d\mu \tag{8}$$

where $\bar{\varepsilon}_{ij}$ and $\bar{\sigma}_{ij}$ denote the components of the volume-averaged strain and stress tensors over the total volume of RVE domain μ, where μ_e is the volume of each element. $\varepsilon_{ij}(x)$ and $\sigma_{ij}(x)$ are the corresponding local strain and stress fields. The equivalent homogenized stiffness tensor C^H_{ijkl} relates the macroscopic quantities via:

$$\bar{\sigma}_{ij} = C^H_{ijkl}\bar{\varepsilon}_{kl} \tag{9}$$

For an orthotropic elastic material, the constitutive relation between stress and strain can be written in matrix notation as:

$$\boldsymbol{\sigma} = \mathbf{C}^{\mathrm{H}}\boldsymbol{\varepsilon} \tag{10}$$

where $\mathbf{C}^{\mathrm{H}}$ is the homogenized stiffness matrix. The inverse of this matrix, $\mathbf{S}^{\mathrm{H}} = (\mathbf{C}^{\mathrm{H}})^{-1}$, is the compliance matrix, from which the effective elastic constants can be extracted using the following relationships:

$$E_i = \frac{1}{S_{ii}},\ \nu_{ij} = \frac{S_{ij}}{S_{ii}}\ (i \neq j),\ G_{ij} = \frac{1}{S_{ij}} \tag{11}$$

where E_1, E_2, and E_3 are the effective Young's moduli along the principal material directions; ν_{12}, ν_{13}, and ν_{23} are the effective Poisson's ratios; and G_{12}, G_{13}, and G_{23} are the effective shear moduli. Details of the volume averaging scheme is further described in Ref. [57,59,61].

Figure 5d presents the computed effective Young's moduli along the principal material directions, normalized by the Young's modulus of the matrix (E_m), as function of normalized RVE size (L/d) for 3 independent mesostructural trials, where L is the edge length of the RVE and d is the maximum length of the largest size of aggregates. The elastic responses observed in smaller RVEs exhibit pronounced orthotropic behavior due to localized heterogeneities and insufficient statistical representativeness. However, as the RVE size increases, the responses along the principal material directions converge, indicating a transition toward isotropic behavior. This trend is consistent with observations in other particulate composite systems, where non-uniform dispersion of discontinuous inclusions leads to effective isotropic elastic properties and stress states when the RVE is sufficiently large [61]. The predicted Young's moduli from our FE mesomechanical models show good agreement with experimental data available in the literature [48,63-66], thereby validating the accuracy of our voxelated mesomechanical representations. Figure 5e also shows the degree of stress non-uniformity within a typical RVE, as revealed by the computed contour distribution.

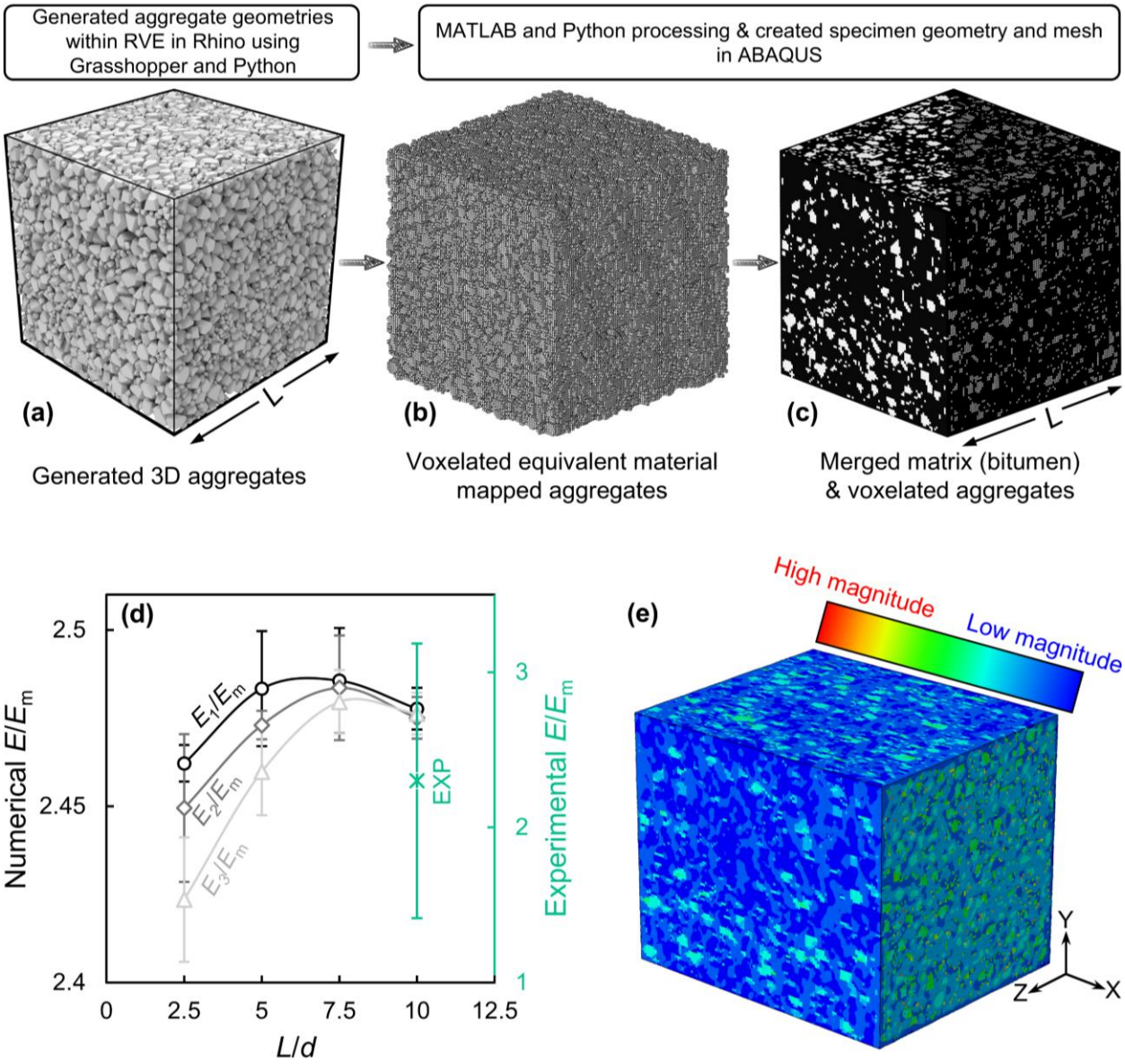

Figure 5: Mesomechanical modeling of asphalt concretes. **(a)** Generated 3D representative volume element (RVE) mesostructure using Rhinoceros 3D and Grasshopper; **(b)** voxelated RVE with equivalent material-mapped aggregates; **(c)** fully merged voxel-based RVE with matrix (bitumen) integrated into the aggregate mesostructure. **(d)** Comparison between experimental elastic moduli and numerical RVE results, showing normalized elastic moduli along three principal directions as function of normalized RVE size (*L*/d); **(e)** typical non-uniform stress distribution within the RVE.

3.3. Fracture test specimen modeling

To examine the influence of mesostructure and specimen geometry on the fracture toughness of aggregate-reinforced construction materials under different loading modes, we used two widely recognized fracture test configurations: the semi-circular bend (SCB) and the edge-notched disc bend (ENDB) specimens (Figure 6a,b). These configurations were used to evaluate fracture behavior under crack opening (Mode I), in-plane shearing or sliding (Mode II), and out-of-plane shearing or tearing (Mode III) conditions [7,10,67,68]. We therefore generated SCB and ENDB specimens with varying aggregate volume fractions of 10%, 20%, 30%, 40%, 50%, and 60% using our mesostructural geometry generation algorithm. Four aggregate size classes were considered: 2.36 mm (size #1), 4.5 mm (size #2), 9 mm (size #3), and 12.5 mm (size #4), with respective volume ratios of approximately 28%, 37%, 26%, and 9% (Figure 6c,d). These aggregate sizes and corresponding volume ratios have broadly utilized in conventional concrete and asphalt mixtures [46-48]. The cases with 0% and 100% aggregate volume fractions represented the homogeneous configurations. The voxelated SCB specimen was modeled with a diameter (D) of 150 mm and a thickness (t) of 50 mm, incorporating 83,440 8-node hexahedral (C3D8R) linear elements and 9,240 20-node hexahedral (C3D20R) quadratic elements. Similarly, the ENDB specimen, with identical dimensions (150 mm diameter (D) and 50 mm height (B)), was voxelated using 54,720 C3D8R linear elements and 7,056 C3D20R quadratic elements (Figure 6e-h). To accurately capture the square-root singularity of the stress and strain fields near the crack front, 20-node hexahedral (C3D20R) quadratic elements were used as singular elements at the crack tip (Figure 6e-h). This was achieved by relocating the mid-side nodes of the first ring of elements surrounding the crack front to one-quarter of the element length away from the crack front nodes, following standard quarter-point techniques [69]. Figure 6g,h indicates that both the aggregate and matrix phases, each with distinct mechanical properties, are incorporated within the singular and non-singular mesh regions in the vicinity of the crack tip.

These specimen dimensions are commonly used in concrete and asphalt mixtures fracture testing, as they conform to the standard dimensions of specimens produced by

the Superpave Gyratory Compactor, a widely adopted device for fabricating cylindrical asphalt samples [70]. The elastic properties of both the aggregate and matrix (bitumen) phases were assigned to be the same as those used in our mesomechanical models. Both SCB and ENDB specimens were loaded under a conventional three-point bending configuration using rigid rollers (Figure 6a,b). All displacement and rotational degrees of freedom of the rigid rollers were constrained, except for the vertical displacement of the loading roller along the loading direction. A general hard contact interaction was defined between the rigid rollers and the specimen surfaces to accurately replicate the loading conditions.

Both SCB and ENDB specimens were modeled with an edge crack initiated from one side, extending through the specimen thickness in the SCB and across the diameter in the ENDB. The crack length was oriented along the specimen radius in the SCB and along the height in the ENDB, as shown in Figure 6a,b. Mode I fracture was simulated by applying symmetric three-point bending, with the distances from the specimen center to the supporting rigid rollers set to S_1=S_2=67.5 mm (S_1/R=S_2/R=0.9) for both SCB and ENDB specimens, where R=D/2 is the specimen radius, and a crack orientation angle was set to α=0°, aligned with the axial direction of the ENDB specimen. Mode II loading was achieved by introducing asymmetry in the supporting rigid rollers: one roller was fixed at S_1=67.5 mm (S_1/R=0.9) in both specimens, while the other was placed closer to the specimen center at S_2=6 mm (S_2/R=0.08) for the SCB specimen, and at S_2=3.81 mm (S_2/R=0.05) with α=0°. Mode III fracture was simulated exclusively in the ENDB specimen by maintaining symmetric supporting rigid rollers at S_1=S_2=71.25 mm (S_1/R=S_2/R=0.95) and rotating the crack about the specimen's axial axis by α=63°. The crack length (a) was set to 30 mm (a/R=0.4) in the SCB specimen, and to 20 mm (a/B=0.4) in the ENDB specimen (Figure 6a,b). The selected loading conditions, crack lengths, and crack orientation angles were based on extensive computational and experimental studies previously reported in the literature for homogeneously assumed materials [71-94], enabling direct comparison between our heterogeneous results and established data. Moreover, these reported configurations have been shown to produce minimal T-stress, thereby reducing the influence of loading type and specimen geometry [18,68]. This

allows for a clearer evaluation of the effects of mesostructure and material heterogeneity, isolated from confounding geometric and loading variables.

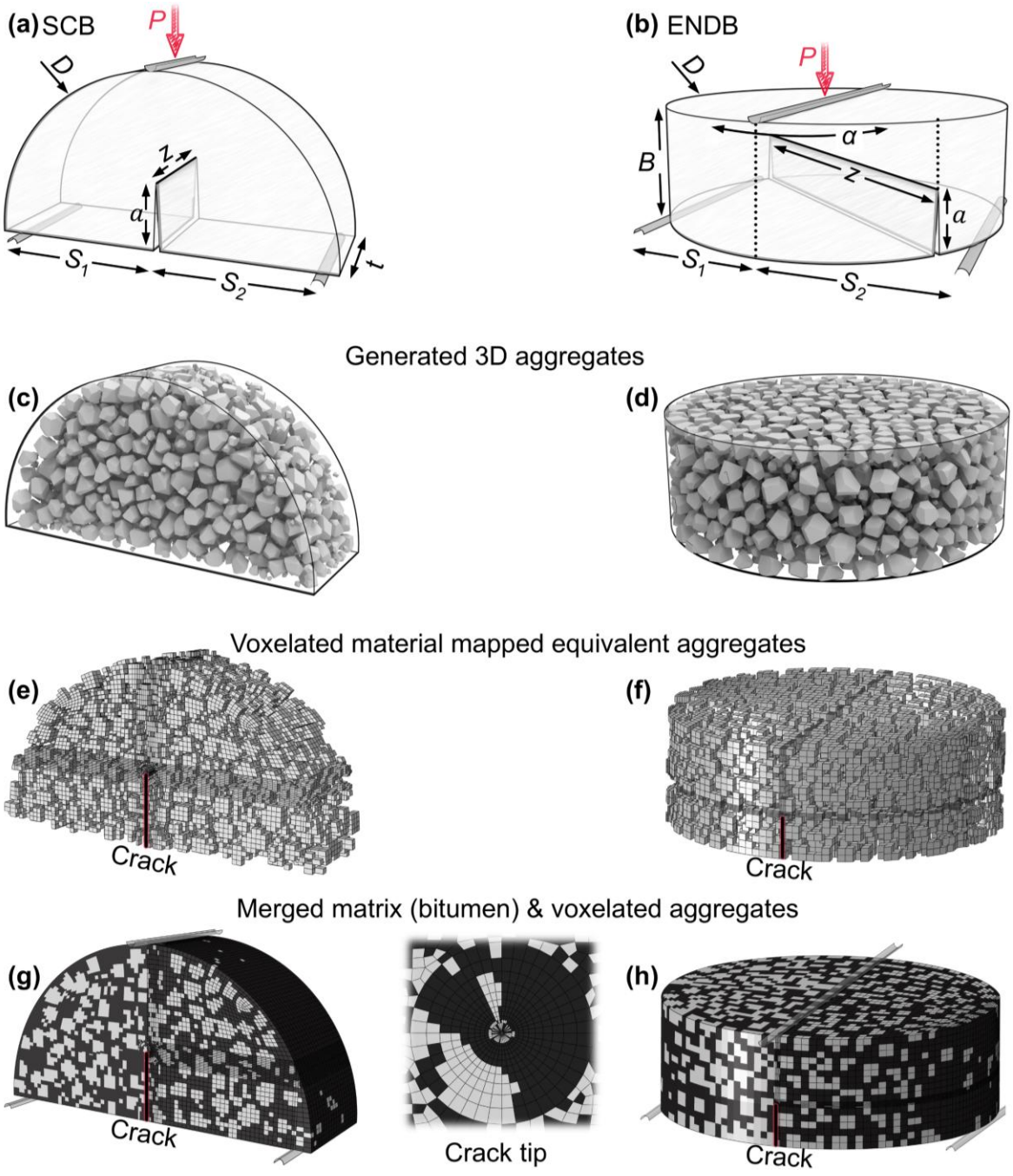

Figure 6: Fracture test specimen mesoscopic modeling. **(a)** Schematic of the semi-circular bend (SCB) and **(b)** edge-notched disc bend (ENDB) specimens and their dimensions. Generated mesoscopic **(c)** SCB and **(d)** ENDB specimens using Rhinoceros 3D and Grasshopper; **(b)** voxelated **(e)** cracked SCB and **(f)** ENDB specimens with equivalent material-mapped

aggregates; **(c)** fully merged voxel-based **(e)** cracked SCB and **(f)** ENDB specimens with matrix (bitumen) integrated into the aggregate mesostructure.

Fracture parameters were computed using a *J*-integral approach, implemented within the ABAQUS, through static analyses of both SCB and ENDB models subjected to different fracture modes. The geometry factors (i.e., Y_{I}, Y_{II}, *and* Y_{III}) were evaluated based on the following general expressions [7,18,68]:

$$K_{\text{I (SCB)}} = \frac{P\sqrt{\pi a}}{2Rt} Y_{\text{I}}\left(a/R,\ S_1/R,\ S_2/R,\ 2z/t,\ V_f\right) \tag{12}$$

$$K_{\text{II (SCB)}} = \frac{P\sqrt{\pi a}}{2Rt} Y_{\text{II}}\left(a/R,\ S_1/R,\ S_2/R,\ 2z/t,\ V_f\right) \tag{13}$$

$$K_{\text{I (ENDB)}} = \frac{3PS_1S_2\sqrt{\pi a}}{RB^2\left(S_1+S_2\right)} Y_{\text{I}}\left(a/R,\ S_1/R,\ S_2/R,\ z/R,\ \alpha,\ V_f\right) \tag{14}$$

$$K_{\text{II (ENDB)}} = \frac{3PS_1S_2\sqrt{\pi a}}{RB^2\left(S_1+S_2\right)} Y_{\text{II}}\left(a/R,\ S_1/R,\ S_2/R,\ z/R,\ \alpha,\ V_f\right) \tag{15}$$

$$K_{\text{III (ENDB)}} = \frac{3PS_1S_2\sqrt{\pi a}}{RB^2\left(S_1+S_2\right)} Y_{\text{III}}\left(a/R,\ S_1/R,\ S_2/R,\ z/R,\ \alpha,\ V_f\right) \tag{16}$$

where P is the applied load, a is the crack length, R is the radius of the specimens, t is the thickness of the SCB specimen and B is the height of the ENDB specimen. $Y_{\text{I (SCB)}}$, $Y_{\text{II (SCB)}}$, $Y_{\text{I (ENDB)}}$, $Y_{\text{II (ENDB)}}$ and $Y_{\text{III (ENDB)}}$ are the geometry factors under Mode I, Mode II and Mode III, for the SCB and ENDB specimens, respectively. They are non-dimensional forms of corresponding $K_{\text{I (SCB)}}$, $K_{\text{II (SCB)}}$, $K_{\text{I (ENDB)}}$, $K_{\text{II (ENDB)}}$ and $K_{\text{III (ENDB)}}$, respectively.

In addition to the geometry factors, *T*-stress is also a critical fracture parameter. The influence of specimen geometry and loading configuration on fracture toughness and fracture initiation angle can be effectively assessed through the inclusion of the *T*-stress term [17,95-97]. The stress and strain fields around a crack tip under general mixed-mode loading can be expressed using the infinite series expansion developed by Williams, as shown below [98]:

$$\sigma_{ij} = \gamma\left(SIF\right) + \xi\left(T\right) + H.O.T \tag{17}$$

where *i* and *j* are *r*, *θ*, and *z* are the local polar coordinates at the crack tip. The first term represents the singular stress field associated with the stress intensity factors (SIFs), while the second term is a non-singular stress component, commonly referred to as the *T*-stress which is independent of the distance from the crack tip. The remaining higher-order terms (H.O.T.) are generally negligible near the crack tip compared to the dominant SIF and *T*-stress terms. At the onset of fracture, the stress at the crack tip reaches a critical value (σ_{cr}), which is considered a material constant. Under such conditions, both the SIFs and *T*-stress attain their critical values. The critical SIFs (e.g., K_{Ic}, K_{IIc} and K_{IIIc}) are typically used as material fracture toughness. However, this assumption is valid only when the *T*-stress is negligible [11,16,18]. If the *T*-stress is non-negligible, its magnitude and sign can significantly influence the apparent fracture toughness—either increasing or decreasing the measured value depending on the mode mixity, specimen geometry and loading configurations [16,17,96,97]. To obtain a valid fracture toughness value that reflects the material property, it is essential to minimize the influence of *T*-stress. Therefore, fracture test configurations that produce near-zero or negligible *T*-stress values are recommended. Under such conditions, the critical SIF becomes directly related to the critical stress ahead of the crack tip, making the measured fracture toughness independent of geometry and loading conditions [16,18]. However, in heterogeneous multiphase materials such as aggregate-reinforced mixtures, mesostructural effects can also play a significant role in influencing the *T*-stress. This additional complexity may affect the measurement of the true material fracture toughness, a factor that has not yet been thoroughly investigated in the literature. In this study, the non-dimensional forms of heterogenous *T*-stress (*T**) under different fracture modes were computed for both SCB and ENDB specimens using the following expressions [7,18,68]:

$$T_{\mathrm{I\,(SCB)}} = \frac{P\sqrt{\pi a}}{2Rt} T_{\mathrm{I}}^{*}\left(a/R,\ S_1/R,\ S_2/R,\ 2z/t,\ V_f\right) \tag{18}$$

$$T_{\mathrm{II\,(SCB)}} = \frac{P\sqrt{\pi a}}{2Rt} T_{\mathrm{II}}^{*}\left(a/R,\ S_1/R,\ S_2/R,\ 2z/t,\ V_f\right) \tag{19}$$

$$T_{\mathrm{I\ (ENDB)}} = \frac{3PS_1S_2}{RB^2\left(S_1+S_2\right)} T_{\mathrm{I}}^{*}\left(a/R,\ S_1/R,\ S_2/R,\ z/R,\ \alpha,\ V_f\right) \tag{20}$$

$$T_{\mathrm{II\ (ENDB)}} = \frac{3PS_1S_2}{RB^2\left(S_1+S_2\right)} T_{\mathrm{II}}^{*}\left(a/R,\ S_1/R,\ S_2/R,\ z/R,\ \alpha,\ V_f\right) \tag{21}$$

$$T_{\mathrm{III\ (ENDB)}} = \frac{3PS_1S_2}{RB^2\left(S_1+S_2\right)} T_{\mathrm{III}}^{*}\left(a/R,\ S_1/R,\ S_2/R,\ z/R,\ \alpha,\ V_f\right) \tag{22}$$

4. Results and discussion

Figure S3a,b (Supplementary Material) presents the typical computed Mode I (Y_{I}) and Mode II (Y_{II}) geometry factors for the SCB specimen as function of the normalized crack front position parameter ($2z/t$) across various aggregate volume fractions. A value of $2z/t=0$ corresponds to the midpoint of the crack front, while $2z/t=\pm1$ represents the crack front endpoints located at the free surfaces. Similarly, Figure S4a-c (Supplementary Material) shows the typical computed Mode I (Y_{I}), Mode II (Y_{II}) and Mode III (Y_{III}) geometry factors for the ENDB specimen versus the normalized crack front position parameter (z/R) across different aggregate volume fractions. Here, $z/R=0$ represents the midpoint of the crack front, whereas $z/R = \pm1$ indicates the crack front endpoints at the free surfaces. Figures S3 and S4 reveal significant differences between the computed geometry factors for the homogeneous cases (0% or 100% aggregate volume fractions) and those for heterogeneous mesostructures with varying aggregate volume fractions, across the entire crack front in both SCB and ENDB specimens under different fracture modes. These nonlinear fluctuations arise from the realistic representation of non-uniformly dispersed aggregates throughout the specimen and more critically, from the explicit incorporation of both material phases—aggregates and matrix, along the crack front. This heterogeneous distribution influences both the far-field stress distribution within the specimen and the local stress concentrations at the crack tip.

Since the base material model used in this study was developed for concrete and asphalt mixtures, we specifically focused on the results corresponding to the 60% aggregate volume fraction, as shown in Figure 7. Figure 7a,b illustrates the homogeneous Mode I

(Y_I) and Mode II (Y_{II}) geometry factors, showing smooth and monotonically converging trends along the normalized crack front position ($2z/t$). However, the computed results near the free surface regions (i.e., $|2z/t| \geq 0.8$ or $|z/R| \geq 0.8$) are not considered valid and must be excluded from the analysis. This limitation arises due to variations in the crack tip singularity in these regions, where classical stress intensity factors are not well-defined because of severe and abrupt changes in the strain gradients, commonly referred to as "corner point singularities" or "free surface effects" [99]. Figure 7c,d presents the computed heterogeneous Mode I (Y_I) and Mode II (Y_{II}) geometry factors for the SCB specimen, evaluated across 3 independent mesostructural trials as function of the normalized crack front position ($2z/t$). The pronounced fluctuations in the results reflect the random distribution of aggregate and matrix phases along the crack front, where the observed peaks correspond to aggregate regions and the valleys to matrix regions or aggregate–matrix interfaces, depending on the local spatial arrangement. Although slight deviations suggest that mesostructural heterogeneity may induce negligible mixed-mode effects, the distinction between Y_I and Y_{II} remains sufficiently pronounced to classify these conditions as representative of Mode I and Mode II conditions, respectively. Figure 7c,d demonstrates the presence of distinct lower and upper bounds along the crack front, which are critical for evaluating heterogeneous fracture toughness. The minimum values correspond to reduced fracture toughness, while the maximum values indicate higher fracture toughness estimates. To enhance the interpretability and practical applicability of these results, we extracted the maximum and minimum values along the crack front and fitted smooth curves through these extrema to define lower and upper bounds, as shown in Figure 7e,f. To further demonstrates how aggregate volume fraction influences the variation of geometry factors along the crack front. We plotted the fitted upper and lower bound curves of the Mode I (Y_I) and Mode II (Y_{II}) geometry factors for the SCB specimen, against the normalized crack front position parameter ($2z/t$) for various aggregate volume fractions as shown in Figure S5a,b (Supplementary Material). The results indicate that the maximum values are consistently located near the midpoint of the crack front.

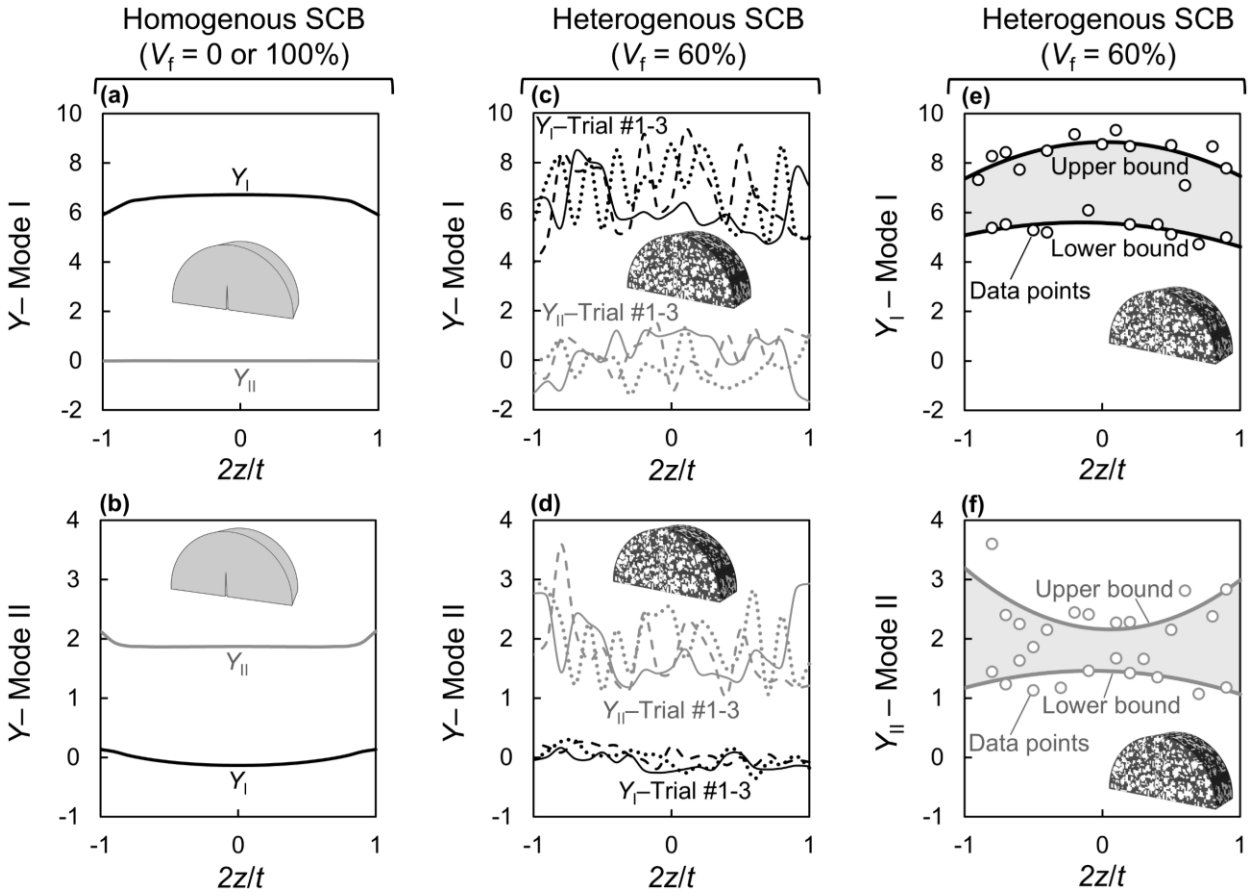

Figure 7: Homogeneous and heterogeneous geometry factors along the crack front ($2z/t$) of SCB specimen. **(a)** Mode I and **(b)** Mode II geometry factors for the homogeneous SCB specimen; **(c)** Mode I and **(d)** Mode II geometry factors for 3 independent mesostructural trials of the heterogeneous SCB specimen; fitted upper and lower bound envelope for **(e)** Mode I and **(f)** Mode II geometry factors in the heterogeneous SCB specimen.

Similarly, Figure 8a–c presents the geometry factors for Mode I (Y_I), Mode II (Y_{II}), and Mode III (Y_{III}) of the homogeneous ENDB specimen as functions of the normalized crack front position (z/R). Figure 8d–f displays the corresponding geometry factors for the heterogeneous ENDB specimen, based on 3 independent mesostructural trials. Figure 8g–i further exhibits the lower and upper bound datasets of geometry factors, along with the corresponding fitted curves, for each of the three fracture modes across the normalized crack front position (z/R) in the ENDB specimen. Figure S6a–c (Supplementary Material) displays the fitted upper and lower bound curves for the Mode I (Y_I), Mode II (Y_{II}), and Mode III (Y_{III}) geometry factors of the ENDB specimen, plotted

against the normalized crack front position (z/R) across different aggregate volume fractions. The results show that, for all studied volume fractions, the peak values of the geometry factors consistently appear near the midpoint of the crack front.

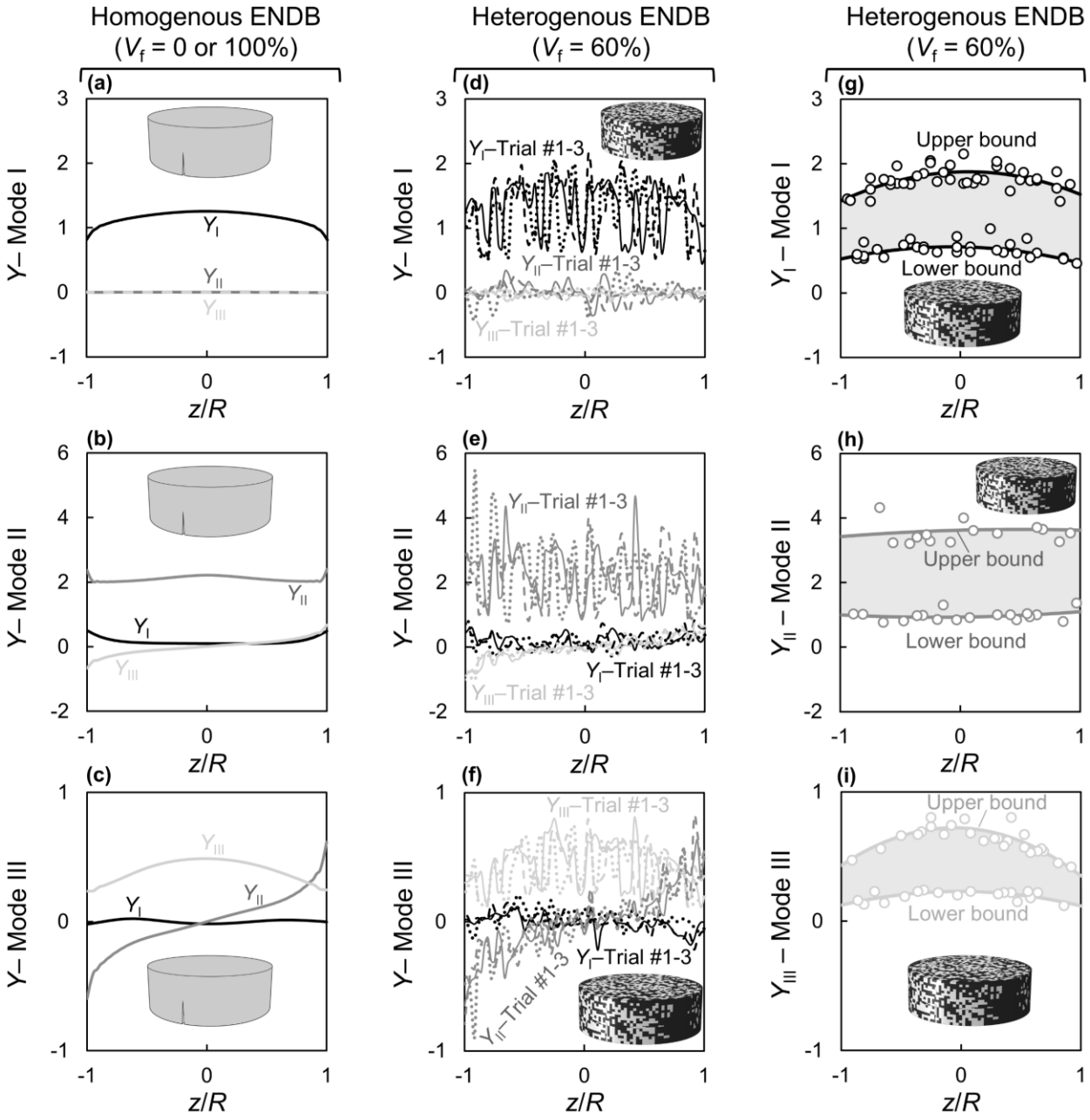

Figure 8: Homogeneous and heterogeneous geometry factors along the crack front (z/R) of ENDB specimen. **(a)** Mode I, **(b)** Mode II, and **(c)** Mode III geometry factors for the homogeneous ENDB specimen; **(c)** Mode I, **(d)** Mode II, and **(e)** Mode III geometry factors for 3 independent mesostructural trials of the heterogeneous ENDB specimen; fitted upper and lower bound

envelope for **(f)** Mode I, **(g)** Mode II, and **(h)** Mode III geometry factors in the heterogeneous ENDB specimen.

Figure 9a,b illustrates the normalized *T*-stress values (*T**) for Mode I and Mode II in the homogeneous SCB specimen, plotted as functions of the normalized crack front coordinate (2*z*/*t*). The corresponding results for the heterogeneous SCB specimens, obtained from 3 independent mesostructural trials, are shown in Figure 9c,d. To better interpret the variability introduced by mesostructural heterogeneity, Figure 9e,f present the extracted lower and upper bounds of *T** along the crack front, with fitted curves highlighting the envelope for *T** each fracture mode. Figure S7a,b (Supplementary Material) present representative normalized *T*-stress (*T**) variations for Mode I and Mode II in the SCB specimen, plotted as functions of the normalized crack front position (2*z*/*t*) across various aggregate volume fractions. In addition, Figure S8a,b (Supplementary Material) display the fitted upper and lower bound curves for the Mode I and Mode II normalized *T*-stress (*T**) values, highlighting the variation of *T** along the crack front for different aggregate volume fractions.

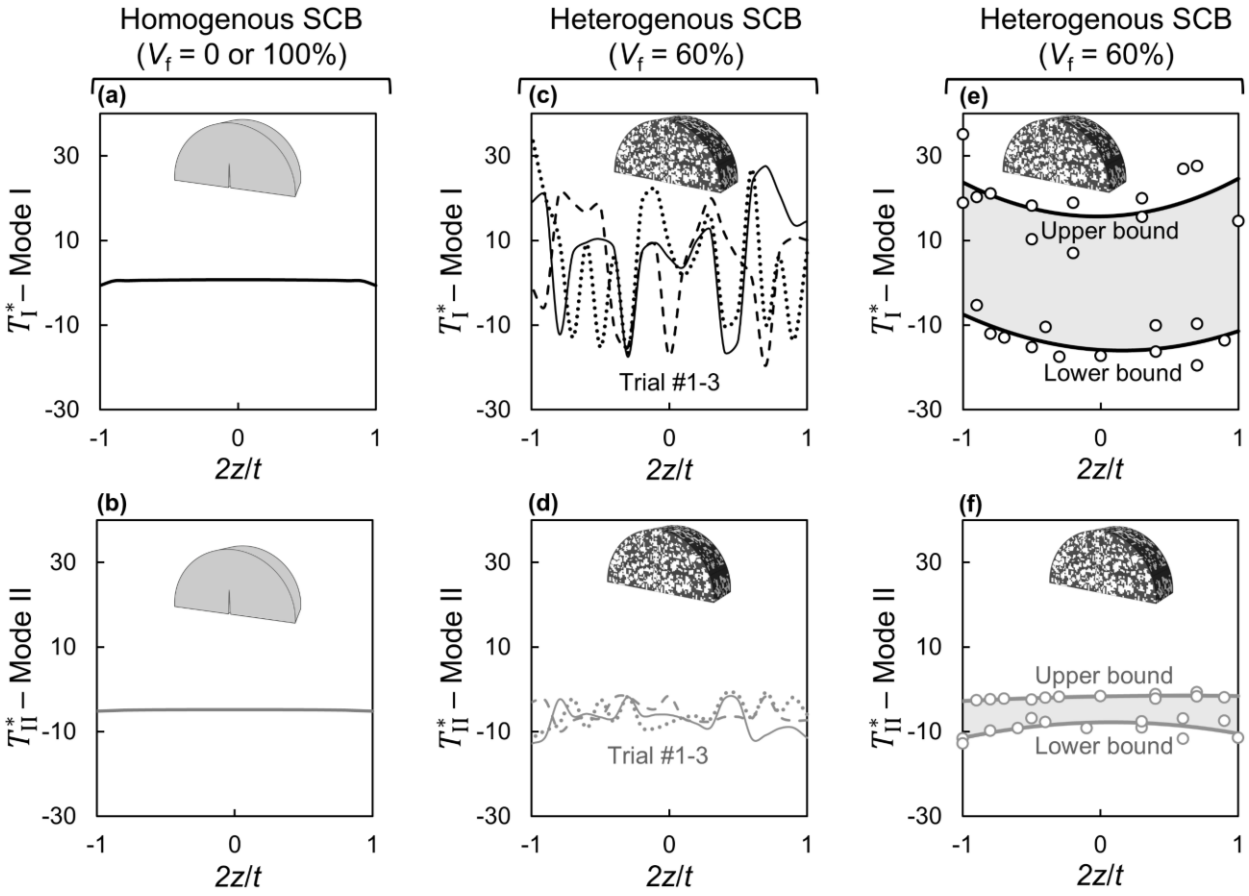

Figure 9: Homogeneous and heterogeneous normalized *T*-stress (*T**) along the crack front (2*z*/*t*) of SCB specimen. **(a)** Mode I and **(b)** Mode II *T** for the homogeneous SCB specimen; **(c)** Mode I and **(d)** Mode II *T** for 3 independent mesostructural trials of the heterogeneous SCB specimen; fitted upper and lower bound envelope for **(e)** Mode I and **(f)** Mode II *T** in the heterogeneous SCB specimen.

An analogous set of results for the ENDB specimen is provided in Figure 10. Specifically, Figure 10a through 10c show the *T** variations under Mode I, Mode II, and Mode III conditions for the homogeneous ENDB, expressed as functions of the normalized crack front coordinate (*z*/*R*). Figure 10d–f displays the corresponding heterogeneous results from 3 independent mesostructures. Finally, Figure 10g–i compiles the lower and upper bound envelopes of *T** for each fracture mode in the ENDB specimen, accompanied by smooth fitted curves that capture the trends across the crack front. Figure S9a–c (Supplementary Material) present typical normalized *T*-stress (*T**) variations for Mode I, Mode II, and Mode III in the ENDB specimen, plotted against the normalized crack front position (*z*/*R*) for a range of aggregate volume fractions. Figure S10a–c (Supplementary Material) also show the fitted upper and lower bound curves through crack front for *T** under each fracture mode for the different aggregate volume fractions.

Figures S5 and S6 show that, in both SCB and ENDB specimens, the upper bound geometry factors across different fracture modes exhibit greater sensitivity to variations in the global aggregate volume fraction (V_f) compared to the lower bound values. In contrast, the heterogeneous *T*-stress components of the SCB specimen demonstrate mixed sensitivities: the lower bound Mode I *T*-stress (T_I^*) and the upper bound Mode II T-stress (T_{II}^*) are less sensitive to changes in V_f. For the ENDB specimen, which features a longer crack front than the SCB specimen, *T*-stress values across all fracture modes are generally less responsive to variations in V_f, with T_{II}^* showing particularly minimal fluctuations.

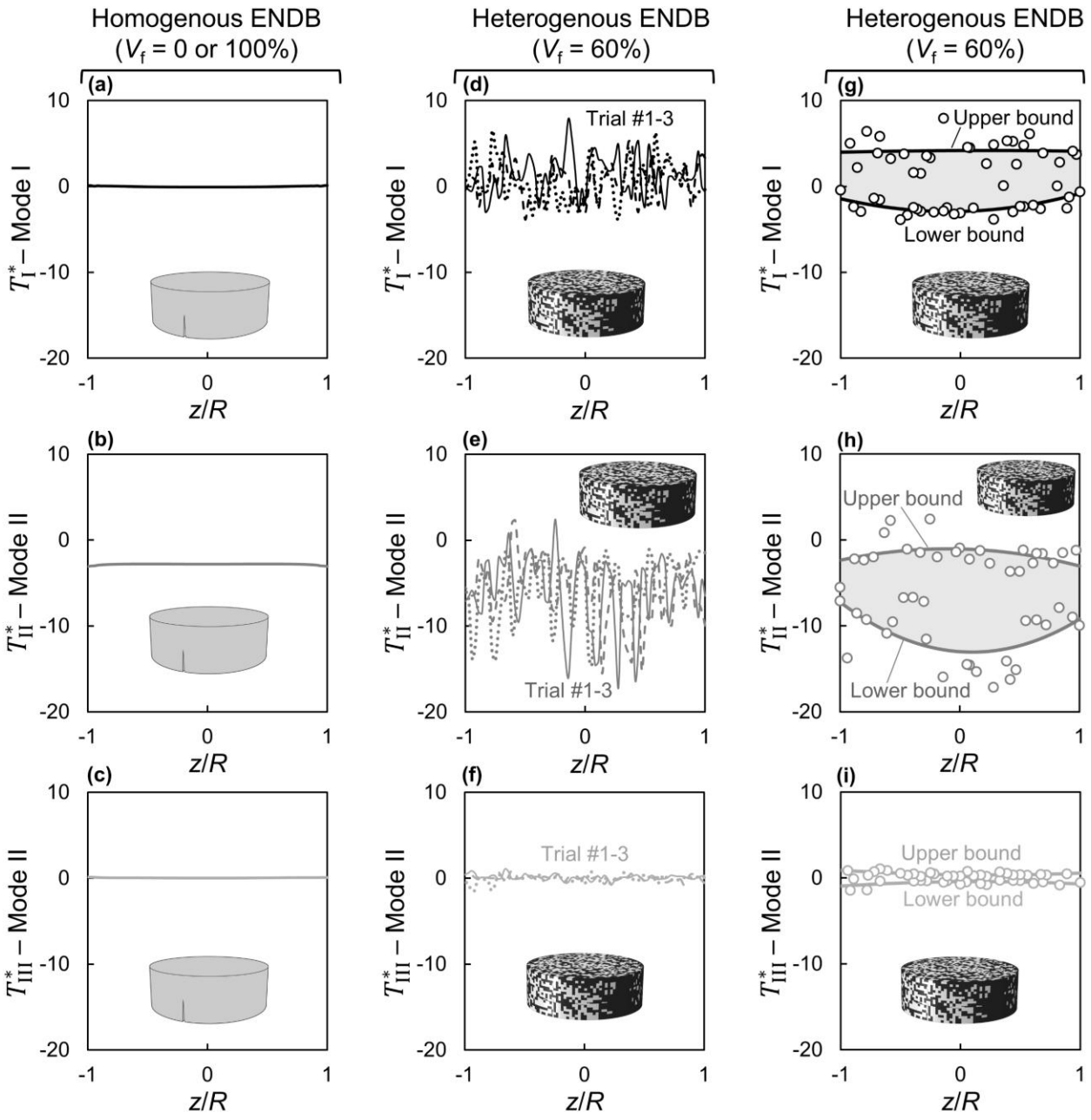

Figure 10: Homogeneous and heterogeneous normalized *T*-stress (*T**) along the crack front (*z*/*R*) of ENDB specimen. **(a)** Mode I, **(b)** Mode II, and **(c)** Mode III *T** for the homogeneous ENDB specimen; **(c)** Mode I, **(d)** Mode II, and **(e)** Mode III *T** for 3 independent mesostructural trials of the heterogeneous ENDB specimen; fitted upper and lower bound envelope for **(f)** Mode I, **(g)** Mode II, and **(h)** Mode III *T** in the heterogeneous ENDB specimen.

To better understand the influence of aggregate and matrix elements along the crack front, we analyzed their local volume fractions. We aimed to confirm that higher geometry factors and *T*-stress upper bounds are associated with aggregate regions, while lower bounds correspond to the matrix phase and interface transitions. To this end, we plotted the fluctuations of Mode I geometry factors (Y_I) and *T*-stress along the crack fronts of both SCB and ENDB specimens (Figure 11a-d). These results are shown alongside the corresponding local aggregate volume fraction (φ_a), defined as follows:

$$\varphi_a\left(2z/t \text{ or } z/R\right) = \frac{V_a\left(2z/t \text{ or } z/R\right)}{V_{Local}\left(2z/t \text{ or } z/R\right)} \tag{23}$$

where φ_a denotes the local aggregate volume fraction at the crack front position ($2z/t$ for the SCB and z/R for the ENDB specimen), with V_a is the aggregate volume at that corresponding local position and V_{Local} is the total local volume at the same location.

Figure 11a–d presents the local aggregate volume fraction (φ_a) alongside the corresponding heterogeneous Mode I geometry factor (Y_I) and *T*-stress profiles along the crack front for both SCB and ENDB specimens, at a global aggregate volume fraction of V_f=60%. The variations in these fracture parameters exhibit a strong correlation with φ_a, confirming that the observed fluctuations primarily result from transitions between aggregate-rich regions and aggregate–matrix interfaces. Similar trends were also observed for Mode II and Mode III fracture parameters, which exhibited strong spatial correlations with φ_a (Figure S11 in Supplementary Material). Notably, the longer crack front in the ENDB specimen increases the likelihood of encountering either fully aggregate or fully matrix segments at a given location, thereby amplifying the microstructural heterogeneity compared to the SCB specimen.

Figures 11e and 11f further demonstrate that the range of heterogeneity—defined by the difference between lower and upper bounds, is significantly larger in the ENDB specimen. This is shown by comparing the heterogeneous Mode I and II geometry factors (Y_I and Y_{II}) normalized by their respective homogeneous values across the crack front. A wider gap between bounds reflects greater heterogeneity. These findings indicate that

specimens with longer crack fronts, such as ENDB, better capture the inherent variability of real-world conditions in aggregate-reinforced materials.

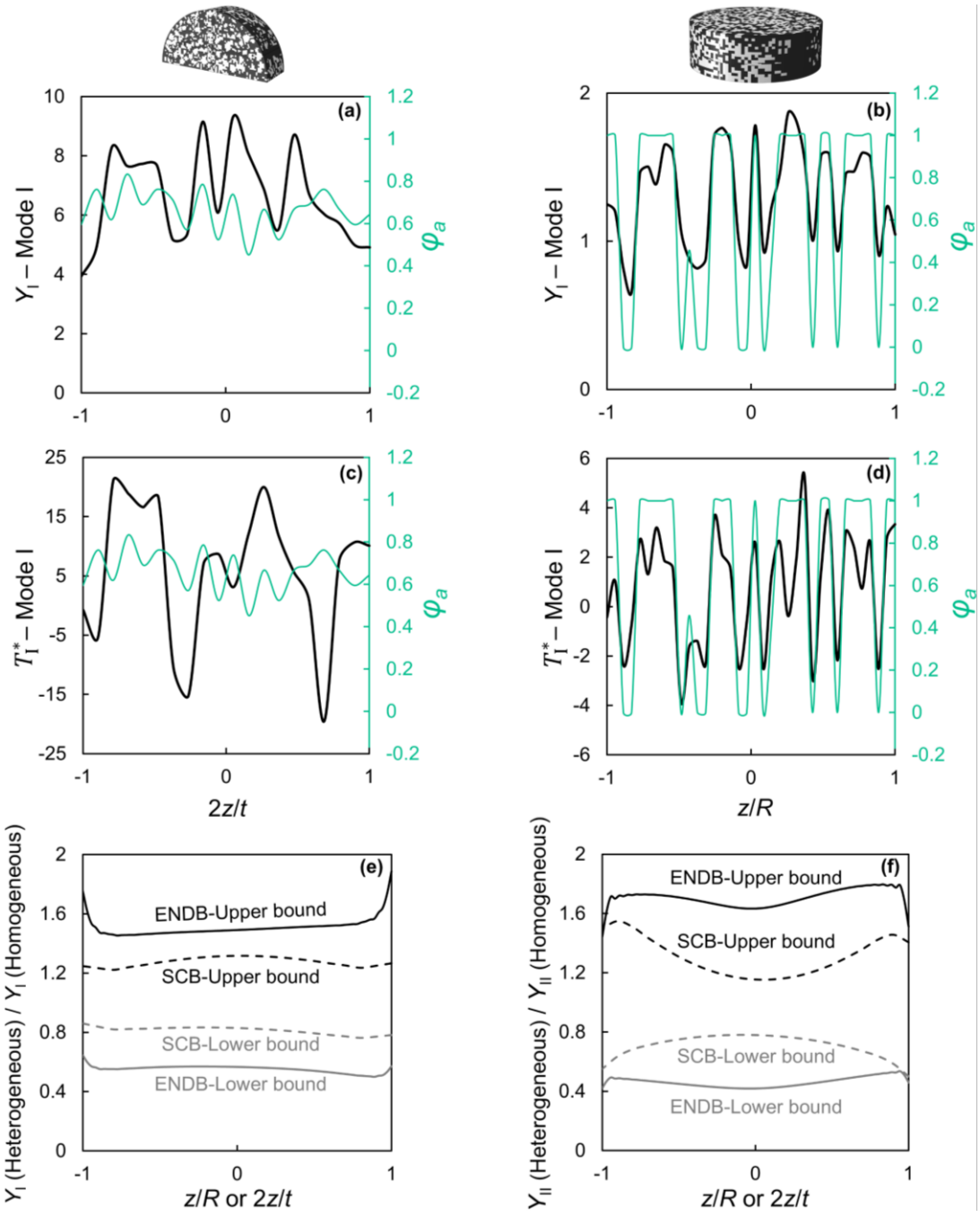

Figure 11: Comparison of mesostructural heterogeneity along the crack front in SCB and ENDB specimens and its influence on fracture parameters. Local aggregate volume fraction (φ_a) and corresponding Mode I geometry factor (Y_I) along the crack front of **(a)** SCB and **(b)** ENDB specimens. Local φ_a and corresponding Mode I *T*-stress across the crack front of **(c)** SCB and **(d)**

ENDB specimens. Normalized lower and upper bound heterogeneous Mode I **(e)** and Mode II **(f)** geometry factors (Y_I and Y_{II}) with respect to their homogeneous counterparts along the crack front.

Based on Figures 7–10 as well as Figures S5 and S6 the extremum points at the lower and upper bounds of geometry factors are consistently located near the midpoint of the crack front in both SCB and ENDB specimens. This observation aligns with the results for homogeneous specimens and is consistent with findings reported in the literature [7,10]. Accordingly, we extracted the lower and upper bound values of geometry factors and *T*-stress at the center of the crack front, corresponding to $2z/t=0$ for SCB and $z/R=0$ for ENDB specimens. To assess the influence of global aggregate volume fraction (V_f) on fracture parameters, we plotted the geometry factors and *T*-stress values at the crack front midpoint across different V_f. Figure 12a,b presents the lower and upper bound geometry factors for SCB and ENDB specimens, respectively, under Mode I, Mode II, and Mode III loading. Here, V_f=0% and 100% represent the homogeneous specimens, while intermediate values of V_f correspond to heterogeneous mesostructures. Similarly, Figure 12c,d shows the corresponding lower and upper bound values of the non-dimensional *T*-stress (T^*) for both specimens under various fracture modes, plotted as functions of aggregate volume fraction, ranging from fully homogeneous to highly heterogeneous configurations.

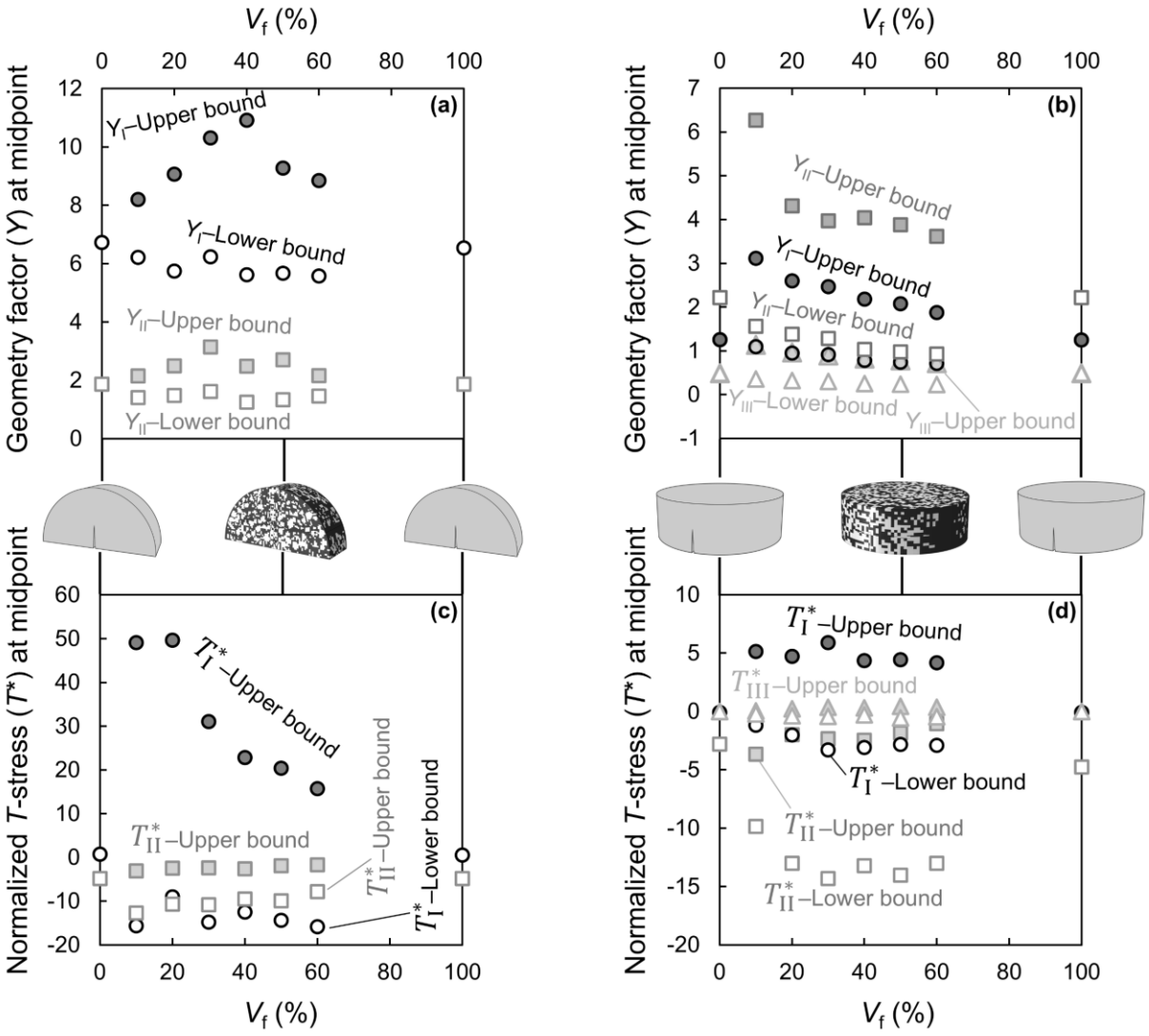

Figure 12: Geometry factors and normalized T-stress (T^*) at the midpoint of the crack front in both SCB and ENDB specimens as functions of global aggregate volume fraction (V_f). Lower and upper bound geometry factors for **(a)** the SCB specimen under Mode I and Mode II loading and **(b)** for the ENDB specimen under Mode I, Mode II and Mode III loading. Lower and upper bound T^* for **(a)** the SCB specimen under Mode I and Mode II loading and **(b)** for the ENDB specimen under Mode I, Mode II and Mode III loading.

We then used the lower and upper bound values of geometry factors and T-stress, computed at the crack front midpoint for V_f=60% (Figure 12), to obtain the heterogenous fracture toughness for asphalt concrete materials under Mode I, Mode II, and Mode III conditions. This was achieved by using the critical fracture loads reported in the literature for SCB and ENDB specimens tested under the same loading modes at low

temperatures. Figure 13 compares the lower and upper bounds of heterogeneous fracture toughness with the corresponding homogeneous values. Figure 13a,b show Mode I (K_{Ic}) and Mode II (K_{IIc}) fracture toughness values for the SCB specimen, respectively. For Mode I, the median lower bound is around 20% below the homogeneous median value, while the median upper bound is about 31% higher, resulting in a total median range of 59%. For Mode II, the median lower bound falls 28% below the homogeneous median value, and the median upper bound exceeds it by 15%, giving a total median variation of 47%.

Figure 13c,d present the Mode I (K_{Ic}), Mode II (K_{IIc}), and Mode III (K_{IIIc}) fracture toughness values for the ENDB specimen. For Mode I, the difference between the median lower bound and the homogeneous median value is approximately 35%, while the difference between the median upper bound and the homogeneous median value is about 48%, resulting in a total difference of 100% between the median lower and median upper bounds. For Mode II, the median lower bound exceeds the homogeneous median value by approximately 138%, and the median upper bound is 63% higher, yielding a total median difference of 289%. For Mode III, the median lower bound is 113% lower than the homogeneous median value, while the median upper bound is 44% higher, giving a total median difference of approximately 208%. Table S1 one summarizes detailed data for the box-and-whisker plots presented in Figure 13. The median percentage differences shown in Figure 13 indicate that the largest deviations between homogeneous and heterogeneous fracture toughness occur in the ENDB specimen across all fracture modes. This may be attributed to the longer crack front in the ENDB specimen, which increases the likelihood of intersecting a greater variety of aggregate-matrix compositions, thereby introducing more pronounced mesostructural heterogeneity along the crack front.

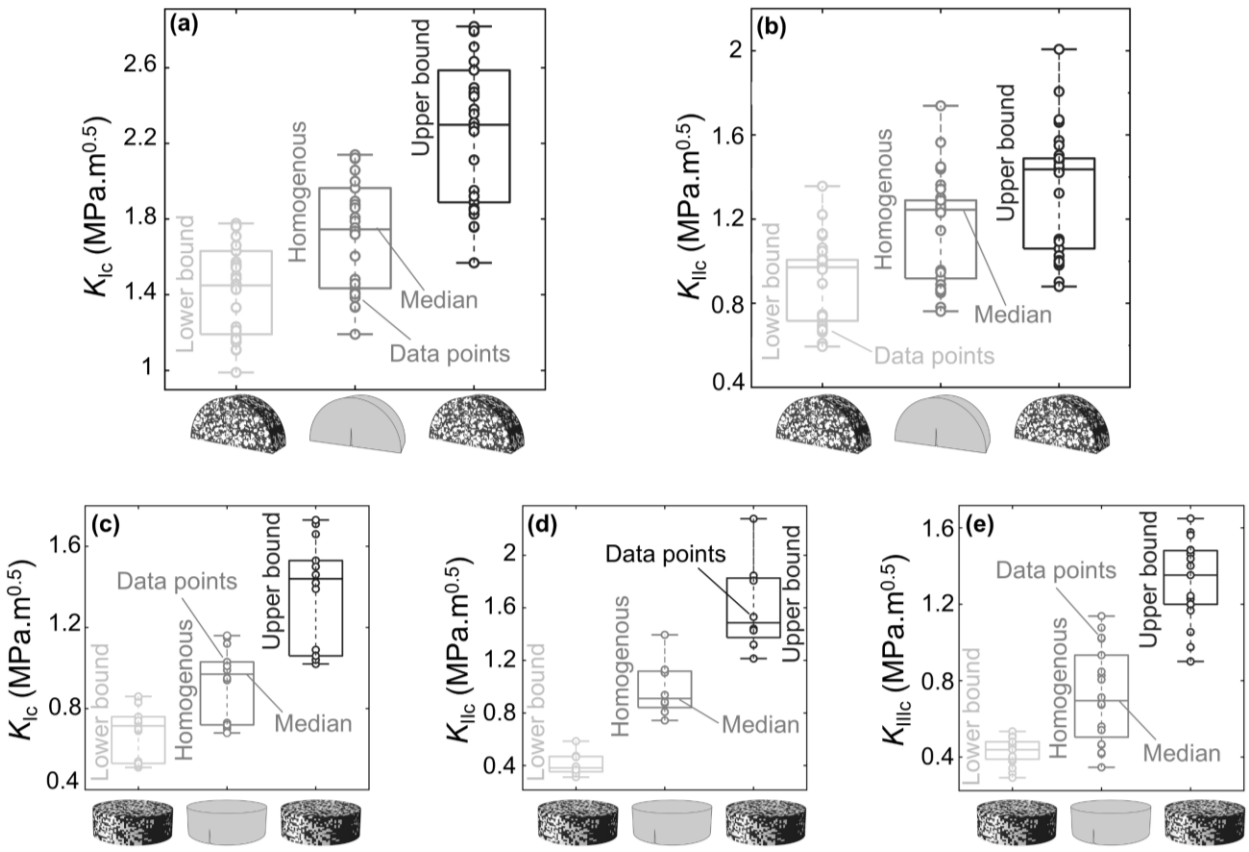

Figure 13: Box-and-whisker plots for the homogenous and heterogeneous fracture toughness of asphalt concretes. **(a)** Mode I (K_{Ic}) and **(b)** Mode II (K_{IIc}) homogenous, lower and upper fracture bound toughness variations of SCB specimen. **(c)** Mode I (K_{Ic}), **(d)** Mode II (K_{IIc}) and **(e)** Mode III (K_{IIIc}) homogenous, lower and upper fracture bound fracture toughness variations of ENDB specimen.

We plotted the obtained homogeneous and heterogeneous fracture toughness values against their corresponding critical *T*-stress to decouple the influence of specimen geometry and mesostructure on the fracture threshold zone of asphalt concretes (Figure 14a-c). Note that the critical *T*-stress values were calculated using the reported critical fracture loads for each test configuration. Figure 14a presents the Mode I fracture toughness (K_{Ic}) as function of the corresponding critical *T*-stress (T_{Ic}). All homogeneous K_{Ic} values occur at $T_{Ic}\approx 0$, indicating that the selected specimen geometry and loading conditions in this study exert minimal influence on the variation of intrinsic fracture toughness. The lower bound K_{Ic}–T_{Ic} values for both specimens exhibit a linear trend on the negative side of T_{Ic}, while the upper bound values align linearly on the positive side.

This distinction highlights the role of mesostructural heterogeneity in defining the Mode I fracture threshold zone for each specimen, as indicated by the shaded regions in Figure 14a. Similarly, Figures 14b and 14c show the K_{IIc}–T_{IIc} and K_{IIIc}–T_{IIIc} relationships, respectively, where the homogeneous, lower bound, and upper bound values follow distinct and aligned linear trends. The shaded regions in these figures emphasize the influence of mesostructural heterogeneity on the Mode II and Mode III fracture threshold zones.

Linear relationships between the lower and upper bounds of heterogeneous fracture toughness and the corresponding critical *T*-stress were derived as follows:

$$K_{Ic}^{LB} = -0.0905T_{Ic} - 0.1095,\ R^2=0.85 \tag{24}$$

$$K_{Ic}^{UB} = 0.1653T_{Ic} - 0.5843,\ R^2=0.95 \tag{25}$$

$$K_{IIc}^{LB}(SCB) = -0.0515T_{IIc} - 0.0735,\ R^2 = 0.96 \tag{26}$$

$$K_{IIc}^{UB}(SCB) = -0.3509T_{IIc} - 0.1088,\ R^2 = 0.96 \tag{27}$$

$$K_{IIc}^{LB}(ENDB) = -0.008T_{IIc} + 0.19,\ R^2 = 0.81 \tag{28}$$

$$K_{IIc}^{UB}(ENDB) = -0.384T_{IIc} + 0.7397,\ R^2 = 0.81 \tag{29}$$

$$K_{IIIc}^{LB}(ENDB) = -0.0733T_{IIIc} + 0.149,\ R^2 = 0.59 \tag{30}$$

$$K_{IIIc}^{UB}(ENDB) = 0.2829T_{IIIc} + 0.4601,\ R^2 = 0.59 \tag{31}$$

where LB stands for lower bound and UP denotes upper bound. These equations enable the conversion of heterogeneous fracture toughness bounds across different specimen types. Specifically, by determining the critical *T*-stress of a given specimen, the corresponding lower and upper bounds of heterogeneous fracture toughness can accurately be estimated.

Based on the observed linear trends and the overlapping fracture threshold zones between the homogeneous and heterogeneous results in Figures 14a–c, we further plotted the heterogeneous fracture toughness values against their corresponding

homogeneous counterparts for Mode I, Mode II, and Mode III, as shown in Figures 14d–f, respectively. The previously reported homogeneous fracture toughness values for asphalt concretes—or future values measured using homogeneous geometry factors, can be recalculated and converted into corresponding lower and upper bound heterogeneous fracture toughness values using the linear relationships derived from the trends shown in Figures 14d–f with R^2=0.99.

$$K_{Ic}^{LB} = 0.8991K_{Ic}^{H} - 0.1277 \quad (32)$$

$$K_{Ic}^{UB} = 1.1923K_{Ic}^{H} + 0.2313 \quad (33)$$

$$K_{IIc}^{LB}(SCB) = 0.7803K_{IIc}^{H} \quad (34)$$

$$K_{IIc}^{UB}(SCB) = 1.1545K_{IIc}^{H} \quad (35)$$

$$K_{IIc}^{LB}(ENDB) = 0.4196K_{IIc}^{H} \quad (36)$$

$$K_{IIc}^{UB}(ENDB) = 1.6331K_{IIc}^{H} \quad (37)$$

$$K_{IIIc}^{LB}(ENDB) = 0.4694K_{IIIc}^{H} \quad (38)$$

$$K_{IIIc}^{UB}(ENDB) = 1.449K_{IIIc}^{H} \quad (39)$$

where LB stands for lower bound, UP denotes upper bound, and H refers to homogenous.

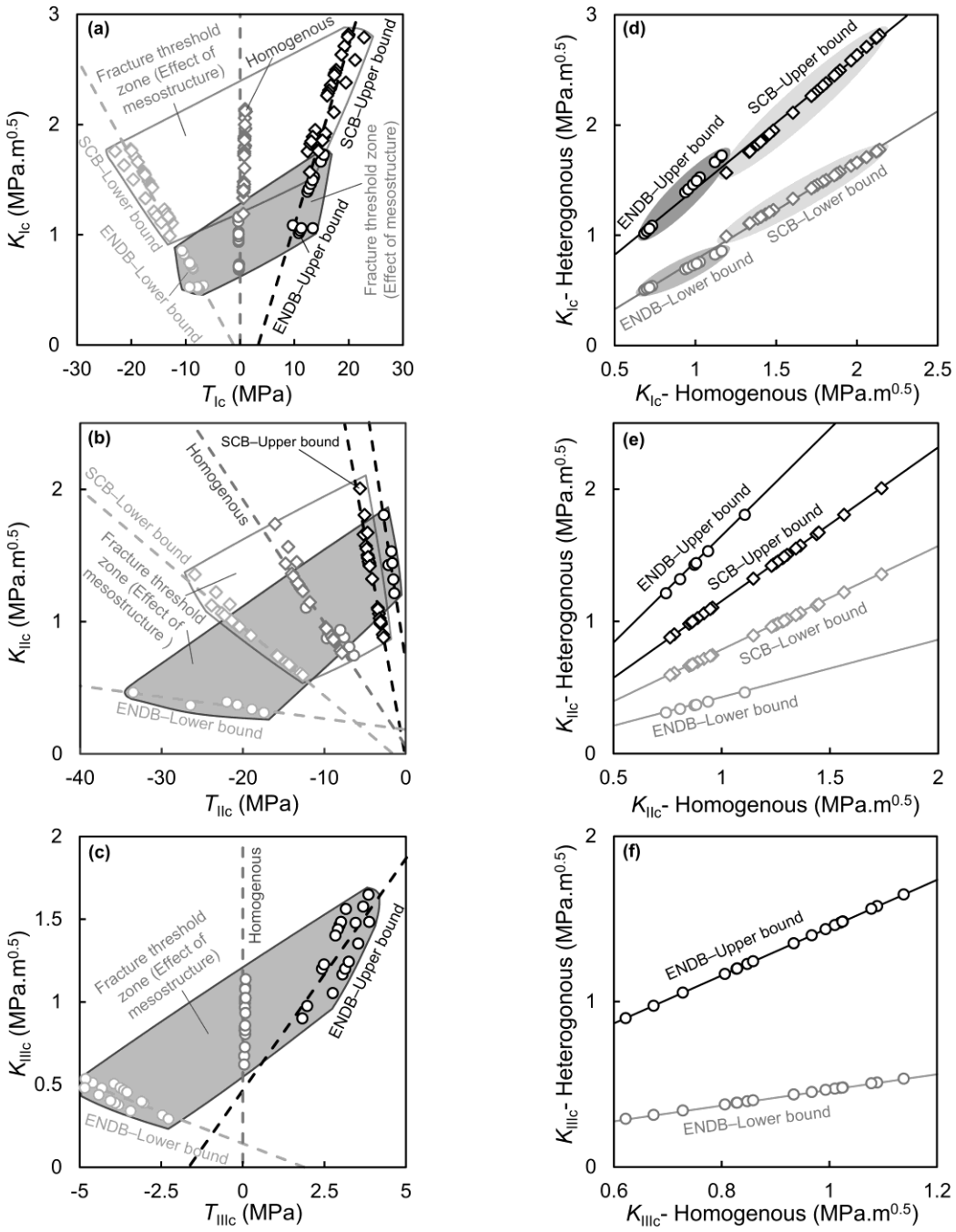

Figure 14: The effect of mesostructural heterogeneity on the fracture threshold zone of asphalt concrete and the relationship between homogenous and heterogeneous fracture toughness for both SCB and ENDB specimens. **(a)** Mode I, **(b)** Mode II, and **(c)** Mode III homogenous, lower and upper bound fracture toughness variations as function of their corresponding critical *T*-stress values. The relation between **(d)** Mode I, **(e)** Mode II, and **(f)** Mode III homogenous with their respective lower and upper bound heterogenous fracture toughness for both SCB and ENDB specimens.

Figure 14 exhibit that the linear relationships between the lower and upper bounds of heterogeneous fracture toughness in ENDB and SCB specimens under Mode I indicate that these properties are not specimen-dependent. They can be interconverted using either the corresponding *T*-stress of a given specimen or the homogeneous fracture toughness. In contrast, Mode II appears to be specimen-dependent, as independent linear relationships were observed for the lower and upper bounds in each specimen type. As for Mode III, further investigation is needed, particularly involving comparisons across different test specimens capable of producing Mode III fracture.

The results underscore that mesostructural heterogeneity is a key nonlinear factor contributing to the wide scatter of fracture toughness values reported in the literature. As such, the fracture toughness of heterogeneous aggregate-reinforced materials cannot be accurately characterized by a single value. Instead, both lower and upper bounds must be considered to fully capture the material's fracture response. To further emphasize the significance of this finding, we introduce and compare the *effective fracture toughness* (K_{eff}) values in Figure 15. These are calculated using the following expressions:

$$K_{eff}^{LB}\left(SCB\right)=\sqrt{K_{Ic-LB}^{2}+K_{IIc-LB}^{2}} \tag{40}$$

$$K_{eff}^{H}\left(SCB\right)=\sqrt{K_{Ic-H}^{2}+K_{IIc-H}^{2}} \tag{41}$$

$$K_{eff}^{UB}\left(SCB\right)=\sqrt{K_{Ic-UB}^{2}+K_{IIc-UB}^{2}} \tag{42}$$

$$K_{eff}^{LB}\left(ENDB\right)=\sqrt{K_{Ic-LB}^{2}+K_{IIc-LB}^{2}+K_{IIIc-LB}^{2}} \tag{43}$$

$$K_{eff}^{H}\left(ENDB\right)=\sqrt{K_{Ic-H}^{2}+K_{IIc-H}^{2}+K_{IIIc-H}^{2}} \tag{44}$$

$$K_{eff}^{UB}\left(ENDB\right)=\sqrt{K_{Ic-UB}^{2}+K_{IIc-UB}^{2}+K_{IIIc-UB}^{2}} \tag{45}$$

where *LB*, *H*, and *UB* represent the lower bound, homogeneous, and upper bound fracture toughness values, respectively.

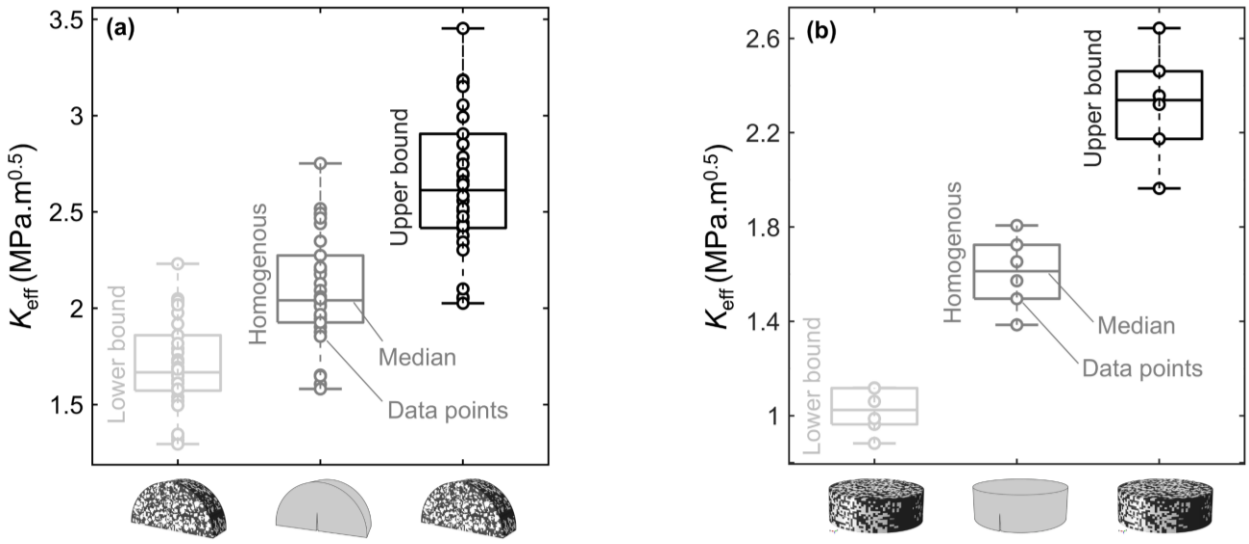

Figure 15: The homogeneous and heterogeneous effective fracture toughness. Homogeneous, lower bound and upper bound effective fracture toughness of **(a)** SCB and **(b)** ENDB.

These expressions provide a framework for evaluating the effective fracture response of heterogeneous material systems by integrating the full range of fracture modes. This approach has practical implications, particularly in estimating the fatigue life of aggregate-reinforced materials such as concrete and asphalt mixtures. For instance, the well-established Paris' law, given by $da/dN = C \cdot (\Delta K)^m$, where da/dN is the crack growth rate, ΔK is the stress intensity factor range, and C and m are experimentally determined material constants, is widely used for fatigue life predictions. In this context, applying conventionally measured fracture toughness values, derived using homogeneous geometry factors and T-stress assumptions, can significantly overestimate fatigue life. In contrast, using the more realistic lower bound heterogeneous fracture toughness values obtained in this study results in notably shorter, and arguably more accurate, fatigue life predictions. This highlights the critical importance of accounting for mesostructural heterogeneity in fracture and fatigue analyses of construction materials.

5. Conclusion

This study introduced a comprehensive and transferable computational framework to quantify the heterogenous fracture toughness of aggregate-reinforced construction materials, using asphalt concretes as a material model system. By explicitly incorporating mesostructural heterogeneity, including aggregate size distribution, shape irregularity, spatial dispersion, and volume fraction—this work addressed key limitations of conventional approaches that rely on homogeneous fracture parameters required for calculating fracture toughness.

A validated 3D aggregate generation algorithm was developed and voxelated into volumetric meshes, enabling distinct material phases to be mapped into finite element models of semi-circular bend (SCB) and edge-notched disc bend (ENDB) specimens. The spatial characteristics of the mesostructures and their mesomechanical responses were rigorously validated through statistical spatial analyses and simulation results, benchmarked against experimental data from the literature. These findings highlight the critical role of mesostructural heterogeneity in defining the fracture threshold zone and mechanical performance of asphalt concretes. The heterogenous fracture threshold zones provide a novel metric for assessing failure risk in multiphase aggregate-reinforced materials.

Concluding remarks include:

- Strong fluctuation in local geometry factors and *T*-stress was observed along the crack front due to random aggregate-matrix distribution.
- Lower and upper bounds of geometry factors and *T*-stress were determined across different aggregate volume fractions, enhancing the general applicability of the modeling framework to other aggregate-based material systems.
- Heterogeneous fracture toughness showed total deviations up to 100% in Mode I, 289% in Mode II, and 208% in Mode III, particularly in ENDB specimens with longer crack fronts.

- Distinct linear relationships were found between fracture toughness and critical *T*-stress, enabling decoupling of geometric effects and mesostructural influence on fracture thresholds.
- Linear transformation functions were derived to convert conventional homogeneous fracture toughness values into upper and lower heterogeneous bounds, allowing reinterpretation of previously published data and guiding future assessments.

In summary, this work delivers a validated and generalizable methodology for characterizing fracture behavior in multiphase aggregate-reinforced material systems. The framework can readily be extended to other material systems such as concrete and polymer composites, informing the design of more durable, fracture-resistant infrastructure materials and supporting more accurate and reliable fracture toughness evaluations as well as test interpretations.

References

[1] Yuan, Q., Liu, Z., Zheng, K., & Ma, C. (2021). Civil engineering materials: from theory to practice. Elsevier.

[2] Khatib, J. (Ed.). (2016). Sustainability of construction materials. Woodhead Publishing.

[3] Al-Atroush, M. E. (2022). Structural behavior of the geothermo-electrical asphalt pavement: A critical review concerning climate change. Heliyon, 8(12).

[4] Kim, K. W., & El Hussein, M. (1997). Variation of fracture toughness of asphalt concrete under low temperatures. Construction and building Materials, 11(7-8), 403-411.

[5] Chen, A., Airey, G. D., Thom, N., Li, Y., & Wan, L. (2022). Simulation of micro-crack initiation and propagation under repeated load in asphalt concrete using zero-thickness cohesive elements. Construction and Building Materials, 342, 127934.

[6] Marasteanu, M. O., Dai, S., Labuz, J. F., & Li, X. (2002). Determining the low-temperature fracture toughness of asphalt mixtures. Transportation Research Record, 1789(1), 191-199.

[7] Aliha, M. R. M., Kouchaki, H. G., & Haghighatpour, P. J. (2023). Designing a simple and suitable laboratory test specimen for investigating the general mixed mode I/II/III fracture problem. Materials & Design, 236, 112477.

[8] Chong, K. P., & Kuruppu, M. D. (1984). New specimen for fracture toughness determination for rock and other materials. International Journal of Fracture, 26(2), R59-R62.

[9] Awaji, H., & Sato, S. (1978). Combined mode fracture toughness measurement by the disk test.

[10] Aliha, M. R. M., Bahmani, A., & Akhondi, S. (2015). Numerical analysis of a new mixed mode I/III fracture test specimen. Engineering Fracture Mechanics, 134, 95-110.

[11] Aliha, M. R. M., Sarbijan, M. J., & Bahmani, A. (2017). Fracture toughness determination of modified HMA mixtures with two novel disc shape configurations. Construction and Building Materials, 155, 789-799.

[12] Becks, H., & Classen, M. (2021). Mode II behavior of high-strength concrete under monotonic, cyclic and fatigue loading. Materials, 14(24), 7675.

[13] Xu, Y., Yao, W., Zhao, G., & Xia, K. (2020). Evaluation of the short core in compression (SCC) method for measuring mode II fracture toughness of rocks. Engineering Fracture Mechanics, 224, 106747.

[14] Wei, M., Dai, F., Liu, Y., & Jiang, R. (2023). A fracture model for assessing tensile mode crack growth resistance of rocks. Journal of Rock Mechanics and Geotechnical Engineering, 15(2), 395-411.

[15] Aliha, M. R. M., & Bahmani, A. (2017). Rock fracture toughness study under mixed mode I/III loading. Rock Mechanics and Rock Engineering, 50, 1739-1751.

[16] Gu, X., Cheng, T., Zhang, F., & Aliha, M. R. M. (2023). Experimental and theoretical framework for illustrating the dependency of fracture toughness with tensile, bending, and compression loading in asphaltic samples. Fatigue & Fracture of Engineering Materials & Structures, 46(9), 3321-3341.

[17] Aliha, M. R. M., Ayatollahi, M. R., & Akbardoost, J. (2012). Typical upper bound–lower bound mixed mode fracture resistance envelopes for rock material. Rock mechanics and rock engineering, 45, 65-74.

[18] Bahmani, A., Farahmand, F., Janbaz, M. R., Darbandi, A. H., Ghesmati-Kucheki, H., & Aliha, M. R. M. (2021). On the comparison of two mixed-mode I+ III fracture test specimens. Engineering Fracture Mechanics, 241, 107434.

[19] Aliha, M. R. M., Ziari, H., Sobhani Fard, E., & Jebalbarezi Sarbijan, M. (2021). Heterogeneity effect on fracture parameters of a multilayer asphalt pavement structure containing a top-down crack and subjected to moving traffic loading. Fatigue & Fracture of Engineering Materials & Structures, 44(5), 1349-1371.

[20] You, T., Al-Rub, R. K. A., Masad, E. A., & Little, D. N. (2013). Three-dimensional microstructural modeling of asphalt concrete by use of X-ray computed tomography. Transportation research record, 2373(1), 63-70.

[21] Aragão, F. T. S., Hartmann, D. A., Pazos, A. R. G., & Kim, Y. R. (2017). Virtual fabrication and computational simulation of asphalt concrete microstructure. International Journal of Pavement Engineering, 18(9), 859-870.

[22] Zhang, H., Ding, H., & Rahman, A. (2022). Effect of asphalt mortar viscoelasticity on microstructural fracture behavior of asphalt mixture based on cohesive zone model. Journal of Materials in Civil Engineering, 34(7), 04022122.

[23] Tan, Z., Leng, Z., Jiang, J., Cao, P., Jelagin, D., Li, G., & Sreeram, A. (2022). Numerical study of the aggregate contact effect on the complex modulus of asphalt concrete. Materials & Design, 213, 110342.

[24] Tan, Z., Yang, B., Leng, Z., Jelagin, D., Cao, P., Li, R., & Zou, F. (2023). Multiscale characterization and modeling of aggregate contact effects on asphalt concrete's tension–compression asymmetry. Materials & Design, 232, 112092.

[25] Zhang, L., Wang, H., & Ren, Z. (2017). Computational analysis of thermal conductivity of asphalt mixture using virtually generated three-dimensional microstructure. Journal of Materials in Civil Engineering, 29(12), 04017234.

[26] Wei, X., Sun, Y., Hu, M., Jiang, F., & Chen, J. (2024). Mesomechanical modeling of asphalt concrete considering full aggregate size range and conjunctive shell mechanism of interface transition zones. Powder Technology, 446, 120155.

[27] Wei, X., Sun, Y., Gong, H., & Chen, J. (2023). Fast 3D voronoi and voxel–based mesostructure modeling method for asphalt concrete. Journal of Engineering Mechanics, 149(9), 04023062.

[28] Naderi, S., Tu, W., & Zhang, M. (2021). Meso-scale modelling of compressive fracture in concrete with irregularly shaped aggregates. Cement and concrete research, 140, 106317.

[29] Wei, X., Sun, Y., Gong, H., Li, Y., & Chen, J. (2023). Repartitioning-based aggregate generation method for fast modeling 3D mesostructure of asphalt concrete. Computers & Structures, 281, 107010.

[30] Sun, Y., Zhang, Z., Wei, X., Du, C., Gong, M., Chen, J., & Gong, H. (2021). Mesomechanical prediction of viscoelastic behavior of asphalt concrete considering effect of aggregate shape. Construction and Building Materials, 274, 122096.

[31] Wei, X., Chen, J., Gong, H., & Sun, Y. (2022). Mesoscopic asphalt pavement response analysis using a random aggregate generation-based concurrent multiscale method. Construction and Building Materials, 321, 126404.

[32] Liang, S., Liao, M., Tu, C., & Luo, R. (2022). Fabricating and determining representative volume elements of two-dimensional random aggregate numerical model for asphalt concrete without damage. Construction and Building Materials, 357, 129339.

[33] Gong, M., Sun, Y., & Chen, J. (2023). Influence of mesoscopic structural characteristics of asphalt mixture on damage behavior of asphalt pavement. Journal of Transportation Engineering, Part B: Pavements, 149(2), 04023007.

[34] Wang, X., Ren, J., Hu, X., Li, Q., & Ji, X. (2023). Meso-scale adhesive/cohesive failure behaviors of porous asphalt mixtures considering random inhomogeneous distribution of binder. Construction and Building Materials, 403, 133097.

[35] Sun, Y., Wei, X., Gong, H., Du, C., Wang, W., & Chen, J. (2020). A two-dimensional random aggregate structure generation method: Determining effective thermo-mechanical properties of asphalt concrete. Mechanics of Materials, 148, 103510.

[36] Song, W., Deng, Z., Wu, H., & Zhan, Y. (2022). Extended finite element modeling of hot mix asphalt based on the semi-circular bending test. Construction and Building Materials, 340, 127462.

[37] Smakosz, Ł., Szydłowski, C., & Górski, J. (2024). Monte Carlo simulations of the fracture resistance of an asphalt pavement layer. Construction and Building Materials, 452, 138970.

[38] Chen, J., Wang, H., Dan, H., & Xie, Y. (2018). Random modeling of three-dimensional heterogeneous microstructure of asphalt concrete for mechanical analysis. Journal of Engineering Mechanics, 144(9), 04018083.

[39] Gong, M., Sun, Y., & Chen, J. (2023). Effect of 3D aggregate shape on thermo-mechanical properties of asphalt concrete using a mesostructure-based homogenisation method. International Journal of Pavement Engineering, 24(2), 2103129.

[40] Qiu, W., Ueda, T., Fu, S., Han, Y., Wang, J., & Ye, J. (2023). Meso-scale computational modeling of the fracture of concrete with complex shaped aggregates under the self-restraint stress. Composite Structures, 303, 116267.

[41] Wei, X., Sun, Y., Gong, H., Li, Y., & Chen, J. (2024). 3D mesomechanical simulation–based approach to determining representative volume element of asphalt concrete. Journal of Transportation Engineering, Part B: Pavements, 150(1), 04024001.

[42] Wei, X., Sun, Y., Gong, H., Zhao, Y., Hu, M., & Chen, J. (2024). 2D aggregate gradation conversion framework integrated with 3D random aggregate method and machine-learning for asphalt concrete. Journal of Materials in Civil Engineering, 36(5), 04024091.

[43] Wei, X., Sun, Y., Gong, H., Hu, M., Zhao, Y., & Chen, J. (2024). Data-mining framework integrating 3D random aggregate method and finite-element method for mesoscopic simulation of asphalt concrete. Journal of Transportation Engineering, Part B: Pavements, 150(3), 04024021.

[44] Wei, X., Sun, Y., Hu, M., & Chen, J. (2025). Three-Dimensional Mesomechanical Complex Modulus Prediction for Asphalt Mortar Considering Conjunctive Shell Mechanism of Interface Transition Zones and Properties of Coarse Mastic. Journal of Engineering Mechanics, 151(2), 04024116.

[45] Gao, L., Zhou, Y., Jiang, J., Yang, Y., & Kong, H. (2024). Mix-mode fracture behavior in asphalt concrete: Asymmetric semi-circular bending testing and random aggregate generation-based modelling. Construction and Building Materials, 438, 137225.

[46] Pour, P. H., Aliha, M. R. M., & Keymanesh, M. R. (2018). Evaluating mode I fracture resistance in asphalt mixtures using edge notched disc bend ENDB specimen with different geometrical and environmental conditions. Engineering Fracture Mechanics, 190, 245-258.

[47] He, J., Liu, L., Yang, H., Aliha, M. R. M., & Karimi, H. R. (2021). Contribution of interface fracture mechanism on fracture propagation trajectory of heterogeneous asphalt composites. Applied Sciences, 11(7), 3013.

[48] Kim, H., & Buttlar, W. G. (2009). Multi-scale fracture modeling of asphalt composite structures. Composites Science and Technology, 69(15-16), 2716-2723.

[49] Wadell, H. (1935). Volume, shape, and roundness of quartz particles. The Journal of geology, 43(3), 250-280.

[50] Wang, X., Guan, Z., Du, S., et al. (2019). A long-range force based random method for generating anisotropic 2D fiber arrangement statistically equivalent to real composites. Composites Science and Technology, 180, 33-43.

[51] Yang, L., Yan, Y., Ran, Z., & Liu, Y. (2013). A new method for generating random fibre distributions for fibre reinforced composites. Composites Science and Technology, 76, 14-20.

[52] Tian, W., Chao, X., Fu, M. W., et al. (2021). An advanced method for efficiently generating composite RVEs with specified particle orientation. Composites Science and Technology, 205, 108647.

[53] Tian, W., Chao, X., Fu, M. W., & Qi, L. (2021). An algorithm for generation of RVEs of composites with high particle volume fractions. Composites Science and Technology, 207, 108714.

[54] Melro, A. R., & Manno, R. (2021). Microscale representative volume element: generation and statistical characterization. In Multi-Scale Continuum Mechanics Modelling of Fibre-Reinforced Polymer Composites (pp. 31-54). Woodhead Publishing.

[55] Younge, K., Christenson, C., Bohara, A., Crnkovic, J., & Saulnier, P. (2004). A model system for examining the radial distribution function. American journal of physics, 72(9), 1247-1250.

[56] Möller, T., & Trumbore, B. (1997). Fast, Minimum Storage Ray-Triangle Intersection. Journal of Graphics Tools, 2(1), 21–28.

[57] Bahmani, A., Li, G., Willett, T. L., & Montesano, J. (2018). Three-dimensional microscopic assessment of randomly distributed representative volume elements for high fiber volume fraction unidirectional composites. Composite Structures, 192, 153-164.

[58] Li, G., Sharifpour, F., Bahmani, A., & Montesano, J. (2018). A new approach to rapidly generate random periodic representative volume elements for microstructural assessment of high volume fraction composites. Materials & Design, 150, 124-138.

[59] Bahmani, A., Li, G., Willett, T. L., & Montesano, J. (2019). Three-dimensional micromechanical assessment of bio-inspired composites with non-uniformly dispersed inclusions. Composite Structures, 212, 484-499.

[60] Bahmani, A., Comeau, P. A., Montesano, J., & Willett, T. L. (2019). Extrudable hydroxyapatite/plant oil-based biopolymer nanocomposites for biomedical applications: Mechanical testing and modeling. Materials & Design, 174, 107790.

[61] Bahmani, A., Nooraie, R. Y., Willett, T. L., & Montesano, J. (2023). A sequential mobile packing algorithm for micromechanical assessment of heterogeneous materials. Composites Science and Technology, 237, 110008.

[62] Jansson, S. (1992). Homogenized nonlinear constitutive properties and local stress concentrations for composites with periodic internal structure. International journal of solids and structures, 29(17), 2181-2200.

[63] Ziari, H., Aliha, M. R. M., Fard, E. S., & Sarbijan, M. J. (2022). Mixed mode I+ II fracture parameters and cracking trajectory of heterogeneous multilayer pavement structure containing reflective crack. Fatigue & Fracture of Engineering Materials & Structures, 45(10), 2958-2977.

[64] Pirmohammad, S., Abdi, M., & Ayatollahi, M. R. (2021). Effect of support type on the fracture toughness and energy of asphalt concrete at different temperature conditions. Engineering Fracture Mechanics, 254, 107921.

[65] LiYongqi, M. (2005). Two—stepapproachtopredictionof asphaltconcretemodulusfrom two—phasemicromechanical models. Journa l ofMater ialin CivilEngineer ing, 17, 407-415.

[66] You, Z., & Buttlar, W. G. (2004). Discrete element modeling to predict the modulus of asphalt concrete mixtures. Journal of materials in civil engineering, 16(2), 140-146.

[67] Bahmani, A., Aliha, M. R. M., Sarbijan, M. J., & Mousavi, S. S. (2020). An extended edge-notched disc bend (ENDB) specimen for mixed-mode I+ II fracture assessments. International Journal of Solids and Structures, 193, 239-250.

[68] Ayatollahi, M. R., Aliha, M. R. M., & Saghafi, H. (2011). An improved semi-circular bend specimen for investigating mixed mode brittle fracture. Engineering Fracture Mechanics, 78(1), 110-123.

[69] Aliha, M. R. M., & Saghafi, H. (2013). The effects of thickness and Poisson's ratio on 3D mixed-mode fracture. Engineering Fracture Mechanics, 98, 15-28.

[70] Fuan, S., Ke, M., Kanghe, L., Kun, L., & Aliha, M. R. M. (2021). Influence of specimen geometry on mode I fracture toughness of asphalt concrete. Construction and Building Materials, 276, 122181.

[71] Pour, P. H., Aliha, M. R. M., & Keymanesh, M. R. (2018). Evaluating mode I fracture resistance in asphalt mixtures using edge notched disc bend ENDB specimen with different geometrical and environmental conditions. Engineering Fracture Mechanics, 190, 245-258.

[72] Motamedi, H., Fazaeli, H., Aliha, M. R. M., & Amiri, H. R. (2020). Evaluation of temperature and loading rate effect on fracture toughness of fiber reinforced asphalt mixture using edge notched disc bend (ENDB) specimen. Construction and Building Materials, 234, 117365.

[73] Fuan, S., Ke, M., Kanghe, L., Kun, L., & Aliha, M. R. M. (2021). Influence of specimen geometry on mode I fracture toughness of asphalt concrete. Construction and Building Materials, 276, 122181.

[74] Zarei, M., Tabasi, E., Ghandehari, M., Rezaie, M., Khordehbinan, M. W., & Al-Bahrani, M. (2022). Effect of hospital waste pyrolysis hydrocarbon (HWPHC) on fracture behavior of Warm Mix asphalt (WMA) under freeze–thaw damage (FTD). Construction and Building Materials, 359, 129473.

[75] Ma, B., Zhou, L., Naseri, A., & Zarei, M. (2025). Improving the short-and long-term cracking behavior of asphalt concrete (AC) under modes III, I/III, and I using New Jig Coal Waste Powder (NJCWP) as a filler replacement. Construction and Building Materials, 476, 141106.

[76] Eghbali, M. R., Tafti, M. F., Aliha, M. R. M., & Motamedi, H. (2019). The effect of ENDB specimen geometry on mode I fracture toughness and fracture energy of HMA and SMA mixtures at low temperatures. Engineering Fracture Mechanics, 216, 106496.

[77] Haghighatpour, P. J., & Aliha, M. R. M. (2022). Effect of marshal and gyratory compaction methods on cracking characteristics of hot mix asphalt concrete materials under all three basic modes of fracture. Theoretical and Applied Fracture Mechanics, 117, 103207

[78] Hajiloo, H. R., Karimi, H. R., Aliha, M. R. M., Zanjirani Farahani, H., Salehi, S. M., Hajiloo, M., & Jafari Haghighatpour, P. (2022). Crack resistance of fiber-reinforced asphalt mixtures: Effect of test specimen and test condition. Fatigue & Fracture of Engineering Materials & Structures, 45(3), 921-937.

[79] He, J., Liu, L., Yang, W., & Aliha, M. R. M. (2022). Influence of testing method on mode II fracture toughness (KIIc) of hot mix asphalt mixtures. Fatigue & Fracture of Engineering Materials & Structures, 45(10), 2940-2957.

[80] Aliha, M. R. M., Bahmani, A., & Akhondi, S. (2016). A novel test specimen for investigating the mixed mode I+ III fracture toughness of hot mix asphalt composites–Experimental and theoretical study. International Journal of Solids and Structures, 90, 167-177.

[81] Motamedi, H., Fazaeli, H., Aliha, M. R. M., & Amiri, H. R. (2020). Evaluation of temperature and loading rate effect on fracture toughness of fiber reinforced asphalt mixture using edge notched disc bend (ENDB) specimen. Construction and Building Materials, 234, 117365.

[82] Haghighatpour, P. J., & Aliha, M. R. M. (2022). Effect of marshal and gyratory compaction methods on cracking characteristics of hot mix asphalt concrete materials under all three basic modes of fracture. Theoretical and Applied Fracture Mechanics, 117, 103207.

[83] Aliha, M. R. M., & Pour, P. J. H. (2020). Fracture resistance study for hot mix asphalt mixture under out of plane sliding mode. Engineering Fracture Mechanics, 238, 107230.

[84] Aalinejadian, H., Aliha, M. R. M., Ameri, M., Karimi, H. R., Jafari Haghighatpour, P., & Choupani, N. (2023). Comparison of mixed mode I/III fracture toughness data obtained from the ENDB specimens manufactured by gyratory cylinders with two diameters of 100 and 150 mm. International Journal of Pavement Engineering, 24(2), 2281996.

[85] Khanghahi, S. H., Irdmousa, P. R., Rezaee, S., Zakavi, S. J., & Shokorlou, Y. M. (2023). Fracture toughness of Gilsonite modified HMA mixtures under mixed mode I/II loading at different temperature conditions. Theoretical and Applied Fracture Mechanics, 127, 104004.

[86] Song, W., Xu, Z., Xu, F., Wu, H., & Yin, J. (2021). Fracture investigation of asphalt mixtures containing reclaimed asphalt pavement using an equivalent energy approach. Engineering Fracture Mechanics, 253, 107892.

[87] Song, W., Yan, W., Wu, H., & Cui, Z. (2025). Investigation of mode I fracture resistance of hot mix asphalt using three testing protocols under the low temperature. Theoretical and Applied Fracture Mechanics, 138, 104937.

[88] Fakhri, M., Siyadati, S. A., & Aliha, M. R. M. (2020). Impact of freeze–thaw cycles on low temperature mixed mode I/II cracking properties of water saturated hot mix asphalt: An experimental study. Construction and Building Materials, 261, 119939.

[89] Aliha, M. M., Behbahani, H., Fazaeli, H., & Rezaifar, M. H. (2014). Study of characteristic specification on mixed mode fracture toughness of asphalt mixtures. Construction and Building Materials, 54, 623-635.

[90] Song, W., Xu, Z., Wu, H., & Zhan, Y. (2022). A novel approach to determine mode II fracture toughness of hot mix asphalt. Theoretical and Applied Fracture Mechanics, 122, 103600.

[91] Fakhri, M., Siyadati, S. A., & Aliha, M. R. M. (2020). Impact of freeze–thaw cycles on low temperature mixed mode I/II cracking properties of water saturated hot mix asphalt: An experimental study. Construction and Building Materials, 261, 119939.

[92] Bazoobandi, P., Karimi, H. R., Mousavi, S. R., Karimi, F., & Aliha, M. R. M. (2023). Full range of mode I and II cracking performance of asphalt mixtures containing low to high reclaimed asphalt pavement (RAP) contents; modified by recycling agent and substituting of a softer binder. Case Studies in Construction Materials, 19, e02487.

[93] Saed, S. A., Karimi, H. R., Rad, S. M., Aliha, M. R. M., Shi, X., & Haghighatpour, P. J. (2022). Full range I/II fracture behavior of asphalt mixtures containing RAP and rejuvenating agent using two different 3-point bend type configurations. Construction and Building Materials, 314, 125590.

[94] Aliha, M. M., Behbahani, H., Fazaeli, H., & Rezaifar, M. H. (2014). Study of characteristic specification on mixed mode fracture toughness of asphalt mixtures. Construction and Building Materials, 54, 623-635.

[95] Smith, D. J., Ayatollahi, M. R., & Pavier, M. J. (2001). The role of T-stress in brittle fracture for linear elastic materials under mixed-mode loading. Fatigue & Fracture of Engineering Materials & Structures, 24(2), 137-150.

[96] Mohammad Aliha, M. R., Ghesmati Kucheki, H., & Asadi, M. M. (2021). On the use of different diametral compression cracked disc shape specimens for introducing mode III deformation. Fatigue & Fracture of Engineering Materials & Structures, 44(11), 3135-3151.

[97] Aliha, M. R. M., Kouchaki, H. G., Mohammadi, M. H., Haghighatpour, P. J., Choupani, N., Asadi, P., ... & Sadowski, T. (2024). Fracture toughness determination for epoxy-based polymer

concrete mixtures: Applicability of different rectangular beam and circular disc specimens. Composites Part C: Open Access, 14, 100446.

[98] Williams, M. L. (1957). On the stress distribution at the base of a stationary crack.

[99] Pook, L. P., Berto, F., & Campagnolo, A. (2017). State of the art of corner point singularities under in-plane and out-of-plane loading. Engineering Fracture Mechanics, 174, 2-9.

Supplementary Material

Heterogeneous fracture toughness of aggregate-reinforced materials via efficient mesoscopic modeling

Aram Bahmani[a], Farzan Farahmand[b], Hadi G. Kouchaki[c,d], Zakiye Nazari[c], Ramin Yousefi Nooraie[e], Mohammad Reza Mohammad Aliha[d,*]

[a] Department of Mechanical Engineering, McGill University, Montreal, Quebec, H3A 0C3, Canada.

[b] Department of Mechanical and Aerospace Engineering, University of Central Florida, Orlando, FL, United States of America.

[c] School of Mechanical Engineering, Iran University of Science and Technology, Narmak 16846-13114, Tehran, Iran.

[d]Welding and Joining Research Center, School of Industrial Engineering, Iran University of Science and Technology, Narmak, 16846-13114, Tehran, Iran.

[e] Department of Mechanical Engineering, Politecnico di Milano, Milano, Italy.

* Corresponding author. Email: mrm_aliha@iust.ac.ir

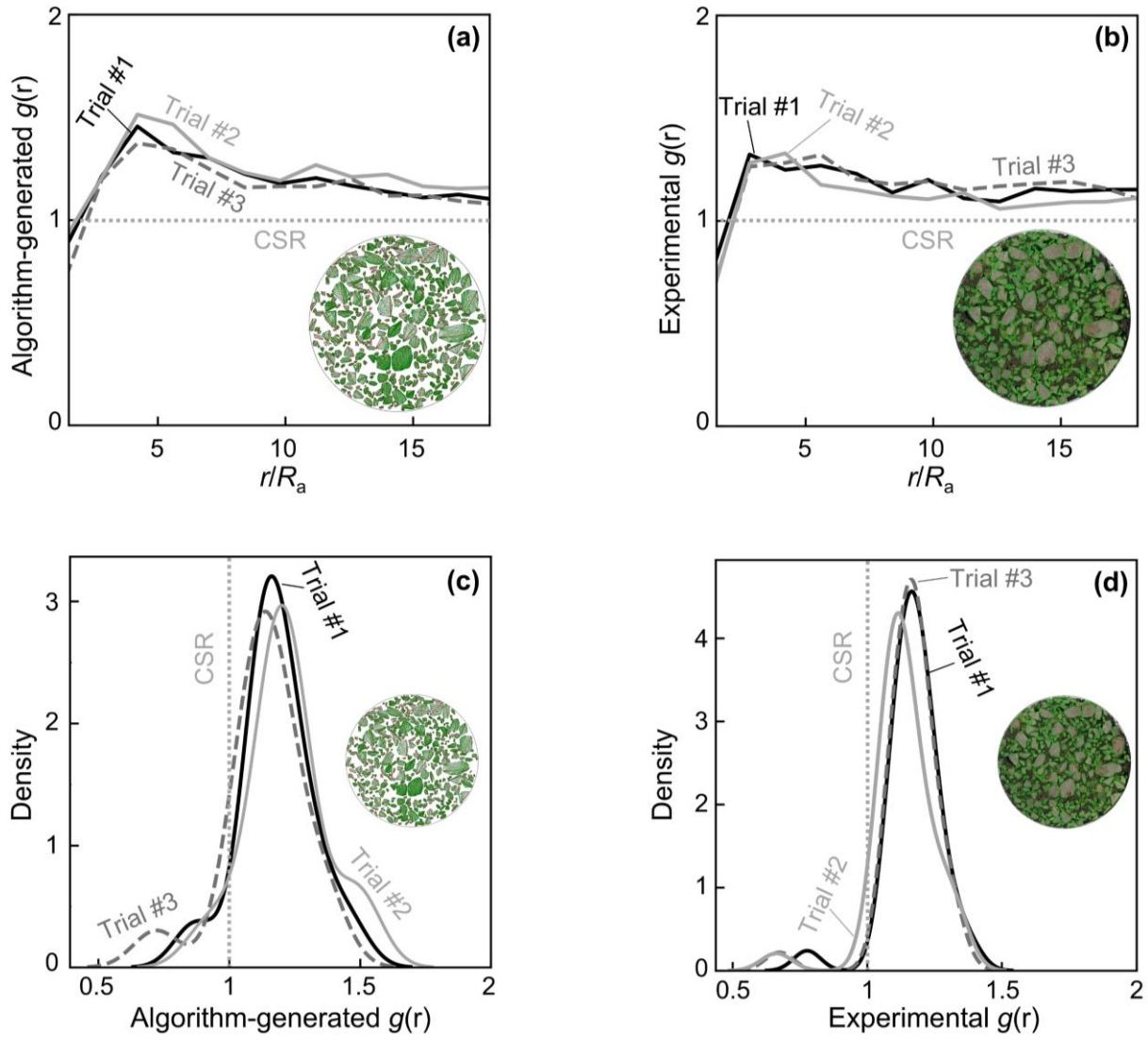

Figure S1: Spatial analysis of experimental and algorithm-generated aggregate distributions, benchmarked against complete spatial randomness (CSR). Radial distribution function *g*(r) of **(a)** algorithm-generated and **(b)** experimental aggregates versus distance normalized by the radius of aggregates (R_a) for 3 independent mesostructure trials. Kernel distribution of the *g*(r) for **(c)** algorithm-generated and **(d)** experimental aggregates for 3 independent mesostructure trials.

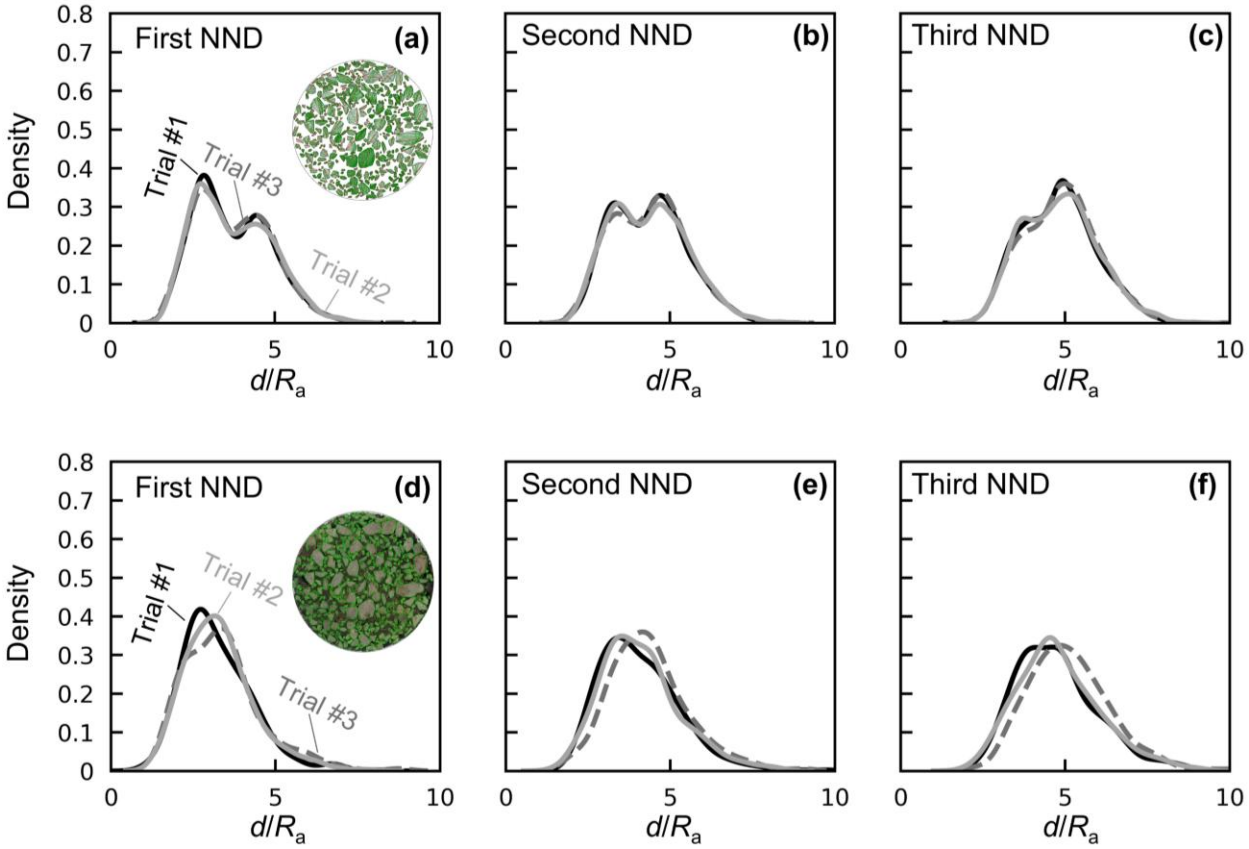

Figure S2: Nearest neighbor distance analysis of experimental and algorithm-generated aggregate distributions. **(a)** First, **(b)** second, and **(c)** third nearest neighbor distance of algorithm-generated aggregates for 3 independent mesostructure trials. **(d)** First, **(e)** second, and **(f)** third nearest neighbor distance of algorithm-generated aggregates for 3 independent mesostructure trials.

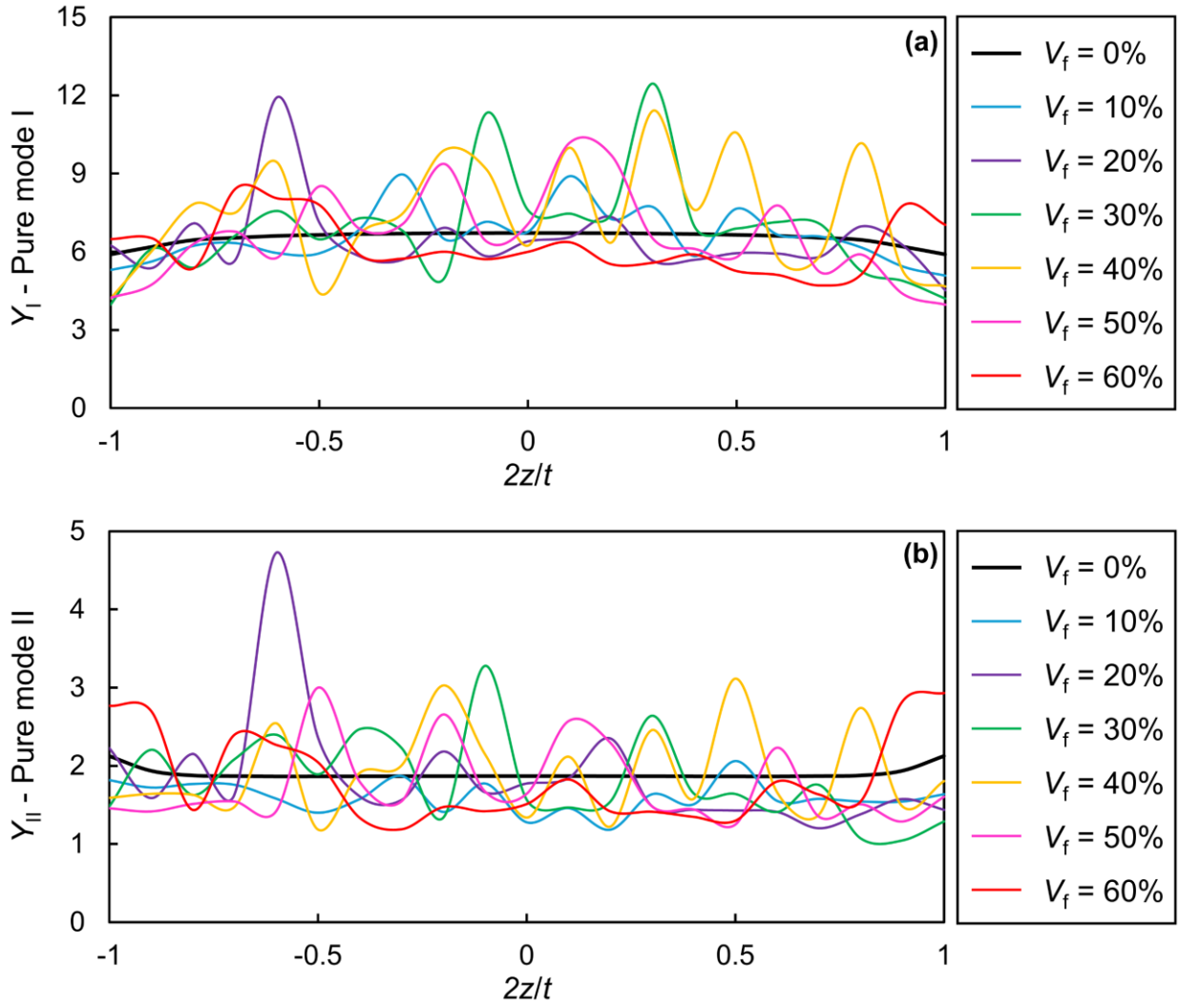

Figure S3: Typical homogeneous and heterogeneous geometry factors along the crack front ($2z/t$) of SCB specimen for different aggregates volume fractions: **(a)** Mode I and **(b)** Mode II.

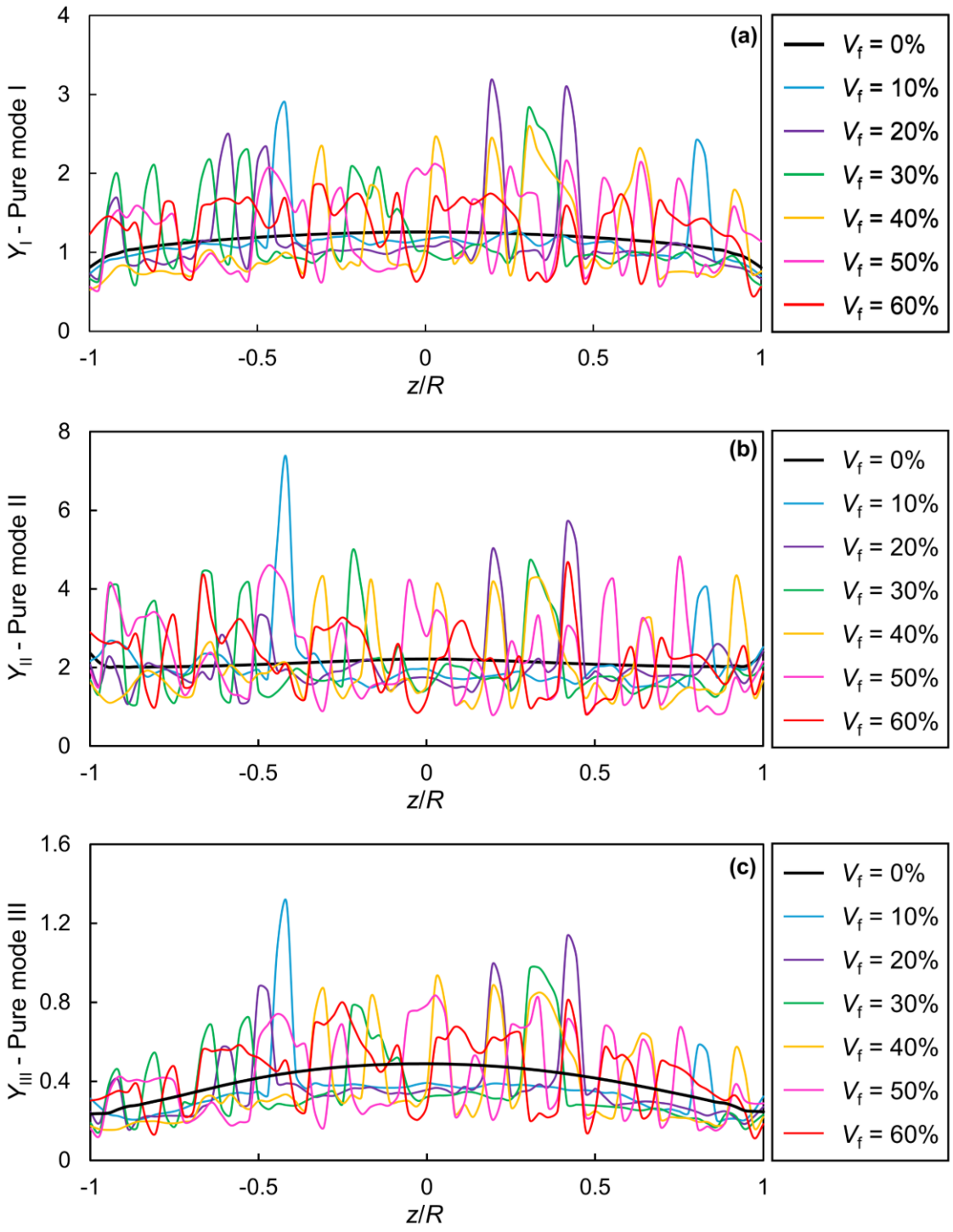

Figure S4: Typical homogeneous and heterogeneous geometry factors along the crack front (z/R) of ENDB specimen for different aggregates volume fractions: **(a)** Mode I, **(b)** Mode II, and **(b)** Mode III.

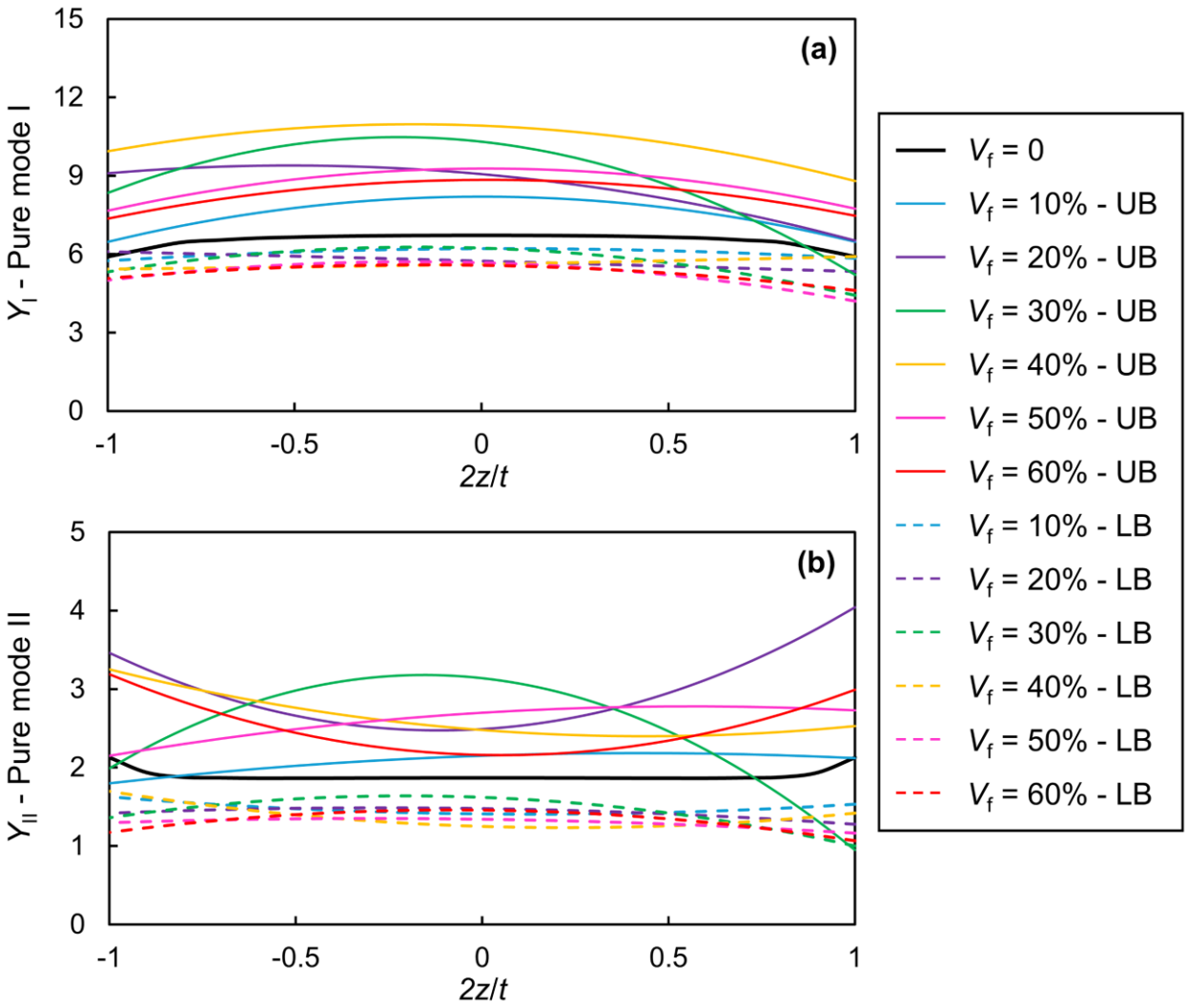

Figure S5: Typical fitted upper and lower bound geometry factor curves along the crack front (2*z*/*t*) of SCB specimen for different aggregates volume fractions: **(a)** Mode and **(b)** Mode II. LB stands for lower bound and UP denotes upper bound.

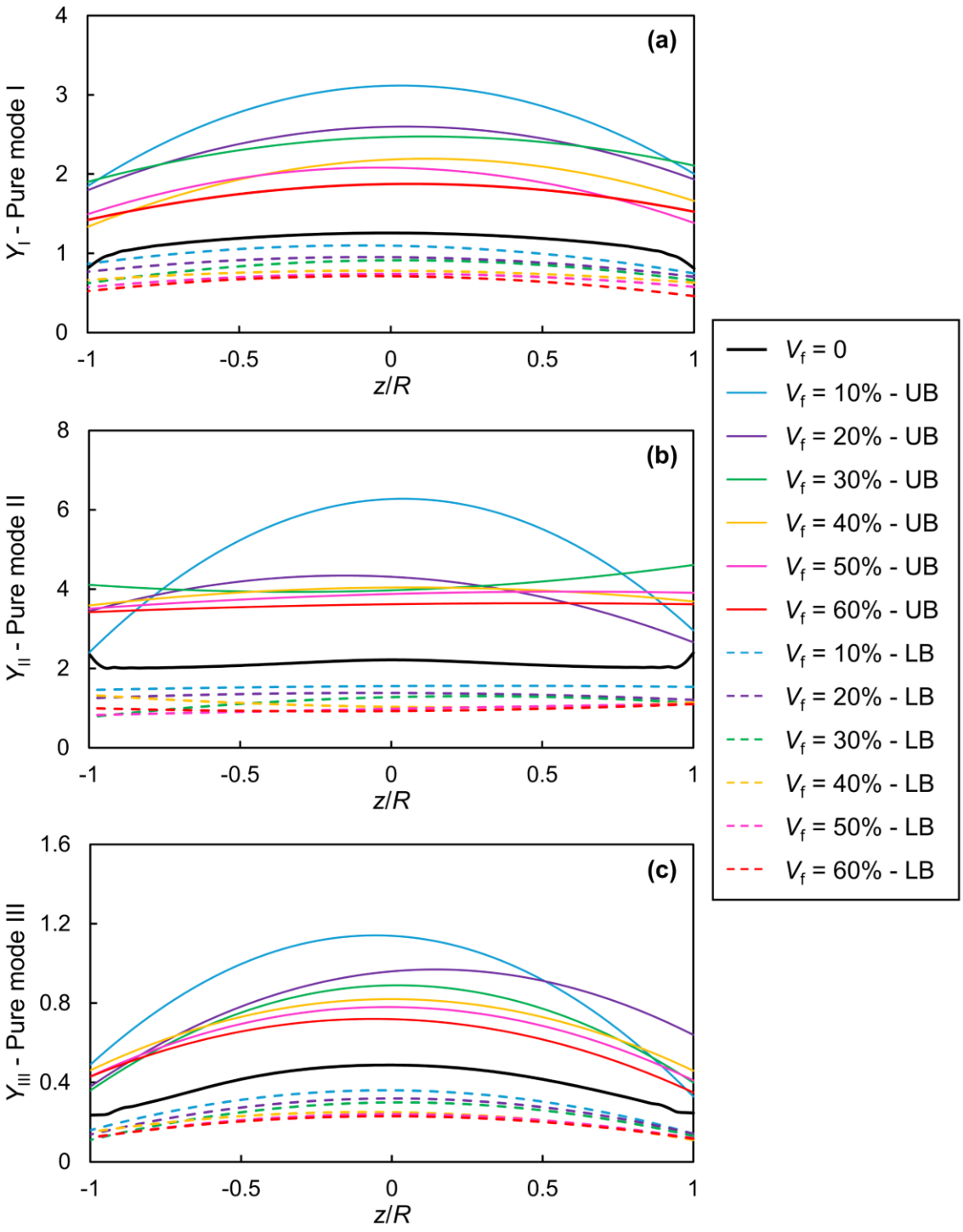

Figure S6: Typical fitted upper and lower bound geometry factor curves along the crack front (z/R) of ENDB specimen for different aggregates volume fractions: **(a)** Mode I, **(b)** Mode II, and **(b)** Mode III. LB stands for lower bound and UP denotes upper bound.

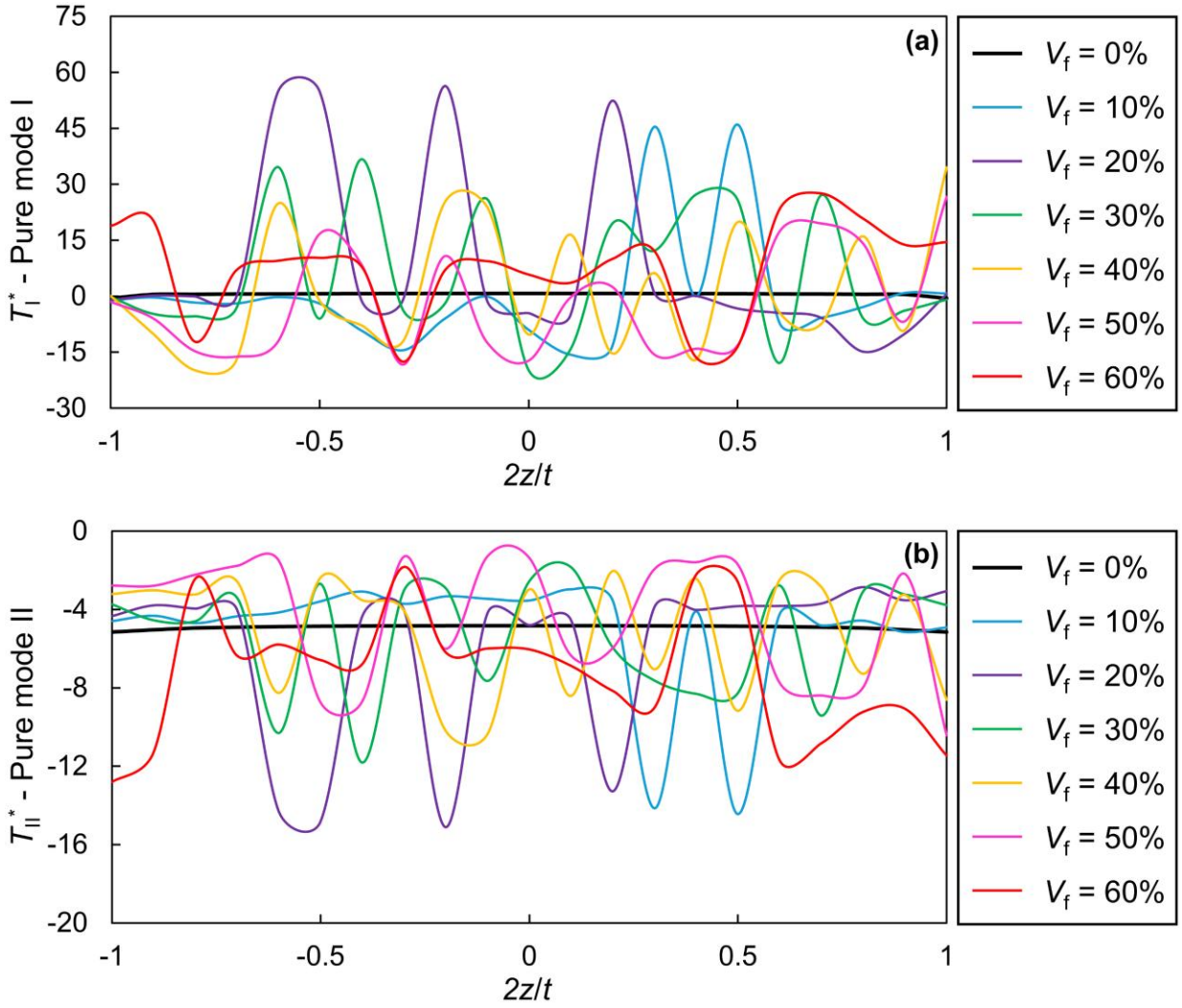

Figure S7: Typical homogeneous and heterogeneous normalized *T*-stress along the crack front (2*z*/*t*) of SCB specimen for different aggregates volume fractions: **(a)** Mode I and **(b)** Mode II.

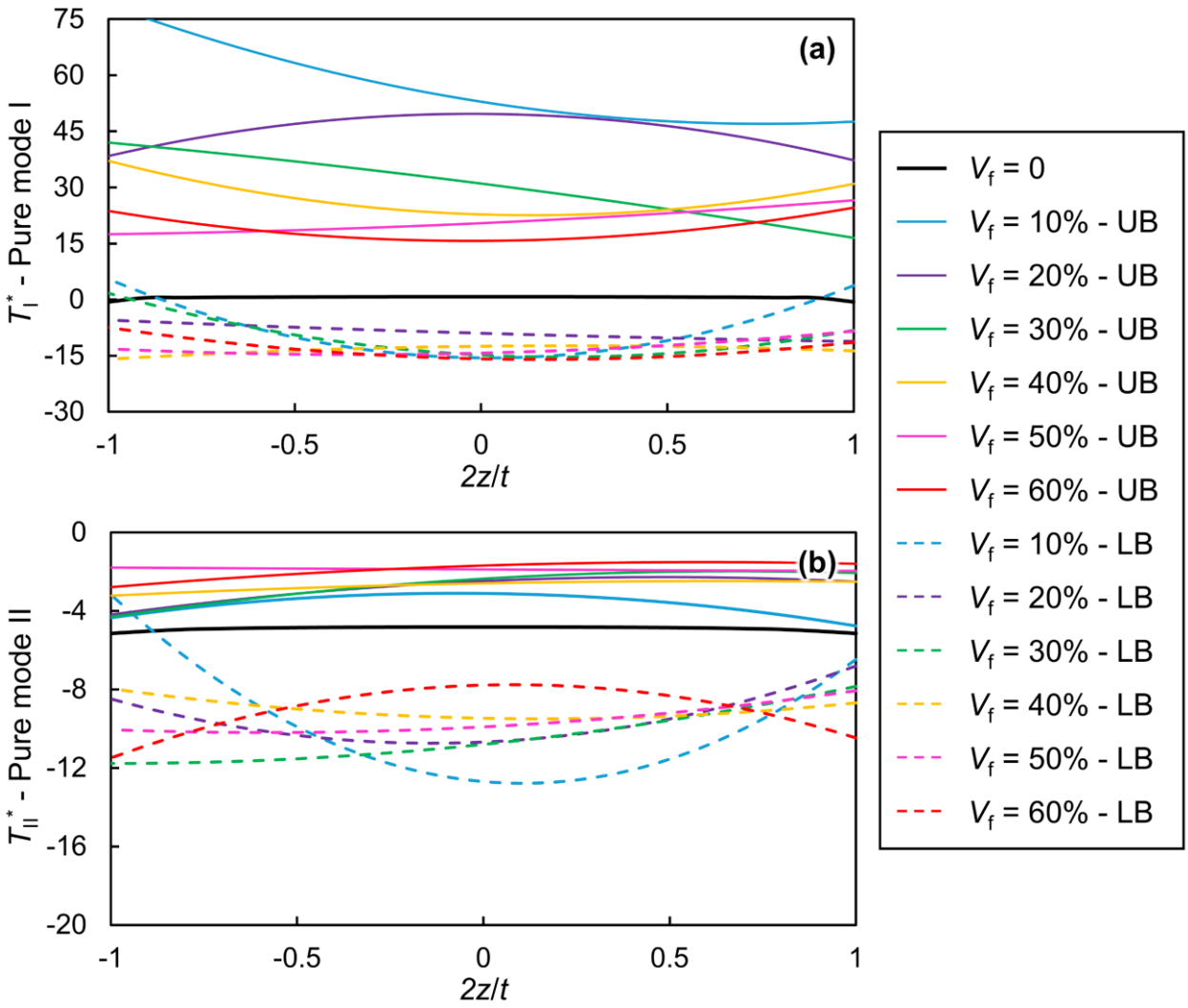

Figure S8: Typical fitted upper and lower bound normalized *T*-stress curves along the crack front (2*z*/*t*) of SCB specimen for different aggregates volume fractions: **(a)** Mode I and **(b)** Mode II. LB stands for lower bound and UP denotes upper bound.

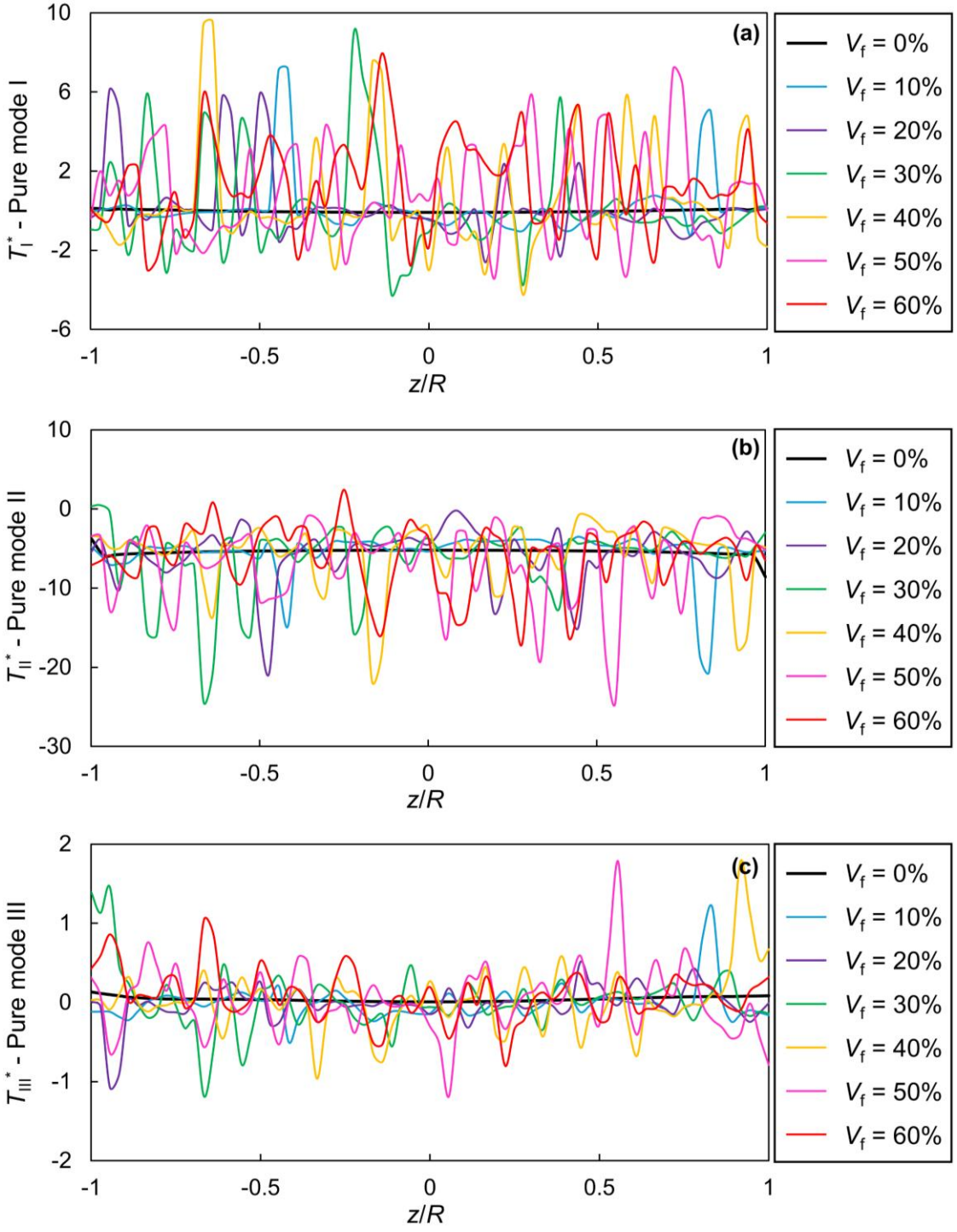

Figure S9: Typical homogeneous and heterogeneous normalized *T*-stress along the crack front (*z*/*R*) of ENDB specimen for different aggregates volume fractions: **(a)** Mode I, **(b)** Mode II, and **(b)** Mode III.

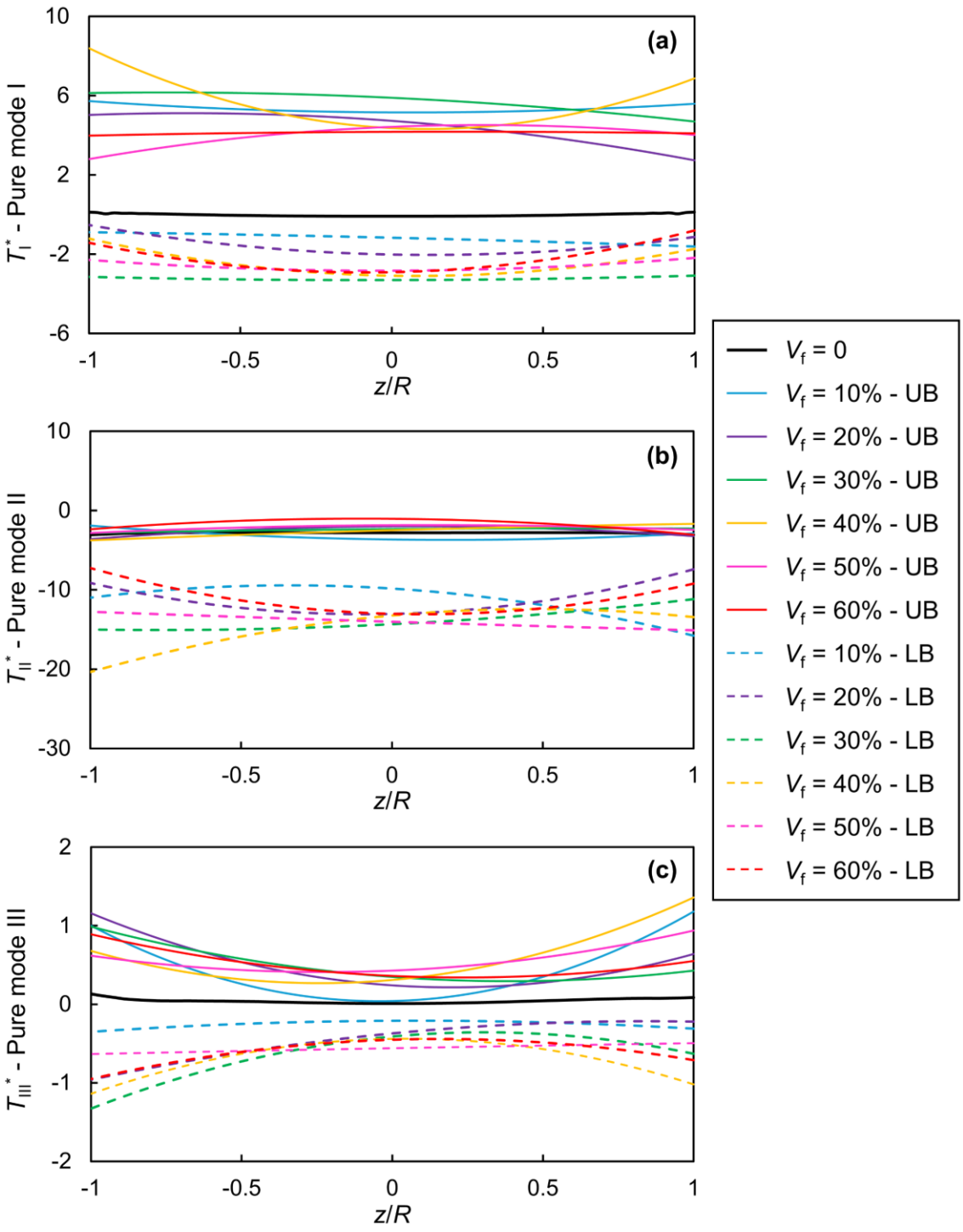

Figure S10: Typical fitted upper and lower bound normalized *T*-stress curves along the crack front (*z*/*R*) of ENDB specimen for different aggregates volume fractions: **(a)** Mode I, **(b)** Mode II, and **(b)** Mode III. LB stands for lower bound and UP denotes upper bound.

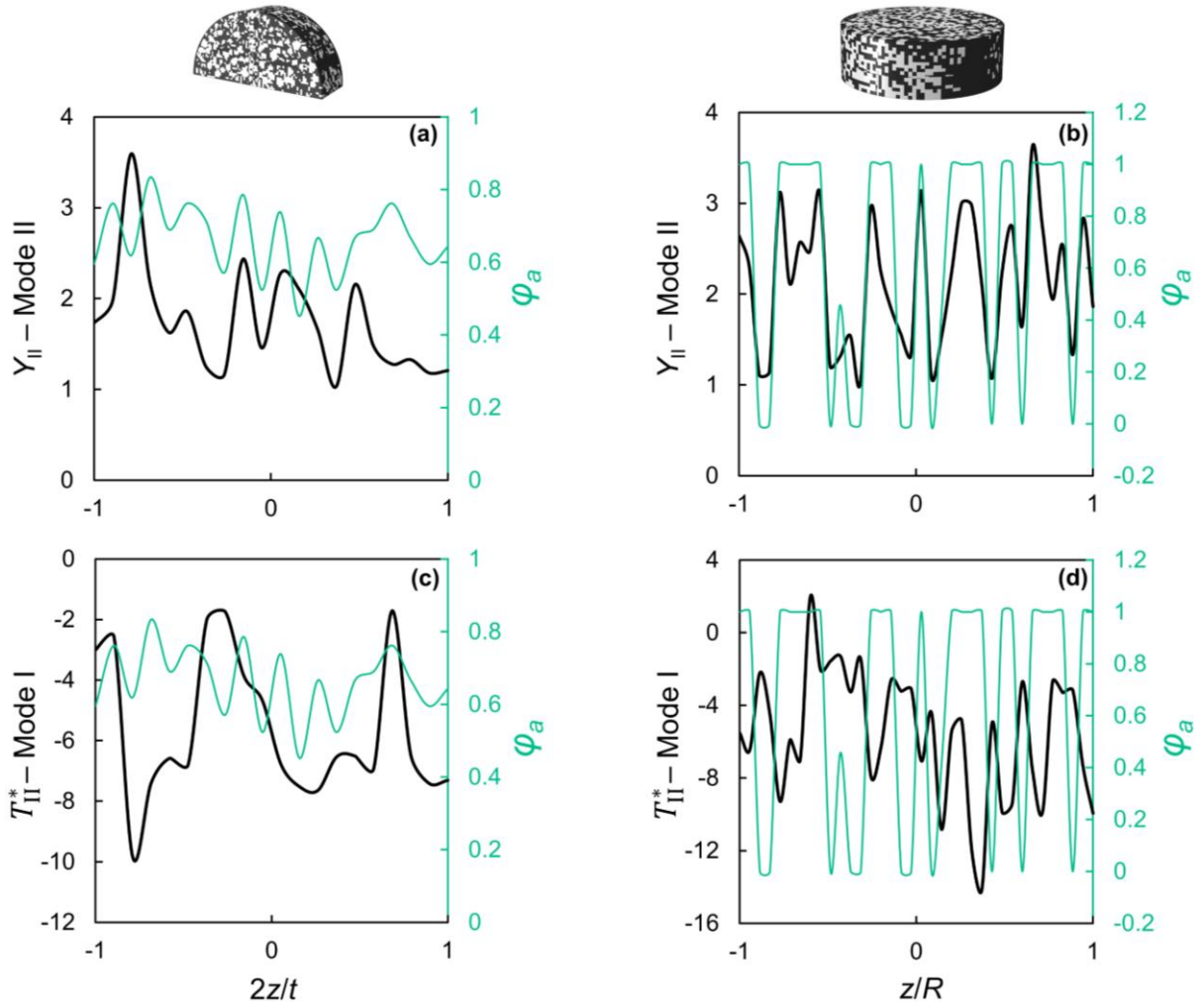

Figure S11: Comparison of mesostructural heterogeneity along the crack front in SCB and ENDB specimens and its influence on fracture parameters. Local aggregate volume fraction (φ_a) and corresponding Mode II geometry factor (Y_{II}) along the crack front of **(a)** SCB and **(b)** ENDB specimens. Local φ_a and corresponding Mode II *T*-stress across the crack front of **(c)** SCB and **(d)** ENDB specimens.